Acta Pharmaceutica Sinica B 2026;16(4):2420−2443

Chinese Pharmaceutical Association
Institute of Materia Medica, Chinese Academy of Medical Sciences

Acta Pharmaceutica Sinica B

www.elsevier.com/locate/apsb
www.sciencedirect.com

ORIGINAL ARTICLE

# From target specificity to metabolic efficiency: Design and optimization of etomidate analogues for potential improvement in postoperative outcomes

**Yi Zhao[a,†], Wei Ai[a,†], Jieyu Zhao[c,†], Xi Yang[d,†], Wencheng Liu[a], Yaru Ma[a], Jianrui Mou[a], Ao Hai[a], Ran Ji[a], Yu Gan[a], Zhuang Miao[a], Shilong Hu[a], Zhenbo Huang[e], Jin Liu[a], Xianggen Liu[a,b,*], Jun Yang[a,*], Bowen Ke[a,e,*]**

[a]*Department of Anesthesiology, Laboratory of Anesthesia and Critical Care Medicine, National-Local Joint Engineering Research Centre of Translational Medicine of Anesthesiology, West China Hospital, Sichuan University, Chengdu 610041, China*
[b]*College of Computer Science, Sichuan University, Chengdu 610065, China*
[c]*West China School of Pharmacy, Sichuan University, Chengdu 610041, China*
[d]*Department of Anesthesiology, Sichuan Provincial People's Hospital, University of Electronic Science and Technology of China, Chengdu 610072, China*
[e]*Key Laboratory of Tropical Biological Resources of Ministry of Education, School of Pharmaceutical Sciences, Hainan University, Haikou 570228, China*

Received 2 July 2025; received in revised form 24 October 2025; accepted 2 December 2025

**KEY WORDS**

Accelerate metabolism clearance;
Intravenous general anesthetic etomidate derivatives;

**Abstract** While transient perioperative side effects of intravenous anesthetics are often tolerated, the persistent postoperative sequelae resulting from drug accumulation pose a critical threat to patient safety. Etomidate, introduced in the 1970s, remains favored for its minimal hemodynamic impact but is severely limited by sustained adrenal suppression, leading to higher mortality and poorer outcomes in critically ill patients. To address these challenges, we reframed our strategy from solely optimizing receptor specificity to enhancing metabolic efficiency, thereby reducing prolonged postoperative exposure and

*Corresponding authors.
E-mail addresses: liuxianggen@scu.edu.cn (Xianggen Liu), yang215jun@163.com (Jun Yang), bowenke@scu.edu.cn (Bowen Ke).
[†]These authors made equal contributions to this work.
Peer review under the responsibility of Chinese Pharmaceutical Association and Institute of Materia Medica, Chinese Academy of Medical Sciences.

https://doi.org/10.1016/j.apsb.2026.01.008

Adrenal cortex function;
Gamma-aminobutyric acid type A receptors;
11$\beta$-hydroxylase;
Soft drug;
Loss of righting reflex;
Recovery of righting reflex

mitigating sustained adverse effects. Using a deep-learning based molecule optimization algorithm, we identified metabolically favorable lead compounds and synthesized 31 novel imidazole-based etomidate derivatives. Among these, ETO-4 emerged as the most promising candidate, retaining potent anesthetic activity while accelerating metabolic clearance and significantly diminishing adrenal suppression. Plasma cortisol assays confirmed the effect of ETO-4 on adrenal function is greatly reduced. These findings underscore a paradigm shift in anesthetic drug design, demonstrating that prioritizing enhanced metabolic profiles can yield safer, more effective agents that improve postoperative outcomes.



## 1. Introduction

General anesthetics are central to contemporary perioperative care, ensuring patient comfort, immobility, and hemodynamic stability throughout surgical procedures. Among intravenous agents, etomidate (ET), first introduced in 1972, has gained widespread clinical use[1-3] due to its favorable hemodynamic profile, making it particularly suitable for patients with cardiovascular instability or cerebrovascular disease[4-6]. However, by 1983, studies revealed that its prolonged adrenal cortical suppression[7,8] and cumulative drug effects could extend postoperative drug exposure and compromise patient safety[9], significantly limiting its clinical utility. Indeed, even single bolus[8] or continuous infusion of ET can significantly inhibit adrenal steroidogenesis, thereby increasing mortality and worsening critical illness severity[9-13].

Mechanistically, ET exerts its anesthetic effects by positively modulating gamma-aminobutyric acid type A receptors ($GABA_AR$)[14-16], while concurrently inhibiting the steroidogenic enzyme 11$\beta$-hydroxylase (CYP11B1), resulting in diminished cortisol synthesis[17-21]. This dual activity is problematic because ET displays approximately 1800-fold greater affinity for CYP11B1 than for $GABA_AR$[22,23], rendering it exceedingly difficult to mitigate adrenal suppression without reducing anesthetic potency. Although previous efforts to improve $GABA_AR$ selectivity have yielded compounds with reduced adrenal inhibition[24,25], these attempts either seriously impair $GABA_AR$ potency or do not improve anesthesia recovery time. For instance, the side effects of carboetomidate have been reduced, but its activity has significantly decreased and the onset time has been significantly prolonged[26]; Although EL-0052 maintained its activity on $GABA_AR$ and reduced side effects, it still failed to improve the recovery time from anesthesia. Therefore, achieving this balance has been a central research focus for the past five decades[17,26-29].

This challenge necessitates a reorientation of the design paradigm. Clinical data indicate that transient perioperative side effects are generally manageable under continuous monitoring, whereas persistent postoperative sequelae stemming from residual drug accumulation significantly threatens patient safety. For etomidate, the minimum plasma concentration needed for anesthesia induction (approximately 200 ng/mL) far exceeds the threshold for adrenal suppression (around 10 ng/mL)[30,31], resulting in prolonged endocrine disturbances. Postoperative adrenal suppression, after continuous infusion of etomidate, can persist beyond 24 h[32]. This suppression is particularly notable in patients with sepsis or trauma, potentially lasting up to 72 h and negatively affecting clinical outcomes[33]. Recognizing that prolonged drug presence rather than initial receptor-specific effects, drives deleterious outcomes, some studies have attempted to modify ET's side chain to facilitate rapid metabolic clearance, thereby shortening this at-risk window. Methoxycarbonyl etomidate (MOC-ET) and cyclopropyl methoxycarbonyl etomidate (CPMM)[34] were designed to be rapidly metabolized, thereby shortening the period of adrenal suppression. However, these compounds have been found to have reduced activity or increased side effects in clinical or preclinical studies. For example, compared with etomidate, the equivalent dose of MOC-etomidate was significantly reduced by approximately 10 times[35]. And the metabolites of them exhibit neurotoxicity or pro-convulsant properties. Animal experiments have shown that CPMM can cause seizures[36], which has raised concerns about the safety and clinical feasibility of these approaches[37].

In the present study, we aimed to overcome these longstanding challenges by leveraging artificial intelligence-assisted drug design to create novel ET-based derivatives with enhanced metabolic properties. By prioritizing accelerated metabolic clearance rather than further receptor-level refinements, our approach seeks to preserve anesthetic potency while attenuating sustained adrenal suppression, thereby offering a promising new avenue for the development of safer and more effective anesthetic agents.

## 2. Results and discussion

### 2.1. Identification of starting scaffold

To enhance the metabolic efficiency of etomidate and minimize its accumulation during continuous infusion, we initially employed a method called Simulated Annealing for Optimization of Graphs and Sequences (SAGS) to optimize the half-life characteristics of etomidate. Using the compound scaffold identified by SAGS, we were able to proceed to screen etomidate derivatives through rational design.

Specifically, SAGS is a topological sampling algorithm in the field of machine learning that enables rapid and efficient exploration of global space. It leverages a pre-trained graph neural network to predict the editing content and adopt simulated annealing to search the optimal molecules by iterative editing[38]. Starting from a given compound to be optimized, SAGS iteratively proposes structural modifications through the insertion, replacement, or deletion of a single atom. The modified compound is then accepted or rejected based on the improvement in its score compared to the original compound. Through this process of random editing and intelligent selection, SAGS gradually generates compounds with the potential to become lead compounds. Specifically, the SAGS framework integrates two key components:

1) Exploration phase: the simulated annealing algorithm stochastically generates diverse molecular modifications to navigate chemical space, guided by a multi-objective fitness function (prioritizing target binding affinity, metabolic stability, and synthetic feasibility). 2) Exploitation phase: intermediate candidates are iteratively filtered using cheminformatics tools (*e.g.*, synthetic accessibility score (SAS), retrosynthetic pathway analysis) to eliminate chemically unstable or synthetically intractable structures. To achieve this objective, we redesigned the target function of SAGS, defining it as a weighted sum of the molecular half-life and the similarity to ET, aiming to preserve the potent anesthetic potency of etomidate while improving metabolic efficiency. Additionally, since the molecules generated by SAGS were entirely novel, determining their half-lives through *in vitro* experiments incurred significant time and labor costs. Therefore, this study employed a random forest regressor to predict the half-life values of the given molecules[39]. Random forest is a simple yet efficient predictive technique in the field of machine learning, capable of training a robust model with minimal labeled data. The structural similarity between any two molecules was assessed by calculating the Tanimoto similarity of their extended connectivity fingerprints (ECFP).

Based on these techniques, the structure of the etomidate molecule was iteratively modified to reduce its half-life while keeping structural changes minimal, ceasing modifications when SAGS no longer alters the structure. Fig. 1A illustrates the optimization process of SAGS, yielding a series of compounds with potential shorter half-lives than etomidate. Meanwhile, we performed molecular docking for all the SAGS-generated intermediate and final candidates to theoretically assess whether they maintained affinities on $GABA_AR$. The results demonstrated that most of these compounds had better docking scores compared to etomidate, indicating that the final candidate SAGS-8 (Supporting Information Fig. S1, renamed as ETO-1 in the following study) may exhibit higher $GABA_AR$ affinities (Fig. 1B). According to SAGS and molecule docking, we identified ETO-1 as an optimal compound, which was predicted to have a half-life 30% shorter than that of etomidate with preserved $GABA_AR$ affinity to keep its anesthetic effect, suitable for clinical situations.

Compound ETO-1 was synthesized and its activity was evaluated *in vitro* and *in vivo*. *In vitro* plasma stability assays revealed complete metabolism of ETO-1 within 20 min, compared to approximately 80% of etomidate remaining unmetabolized after 60 min. While absolute predicted *vs*. observed half-life values showed minor deviations (likely due to limitations in the training dataset's size), the rank-order consistency was preserved: ETO-1's predicted half-life was shorter than ET's, aligning with experimental trends. This validates the utility of our predictor in guiding the SA search toward the desired pharmacokinetic profile.

Also, ETO-1 exhibited significantly less inhibition of human CYP11B1 than etomidate ($IC_{50}$: ETO-1 *vs*. ET: 2.92 *vs*. 0.94 nmol/L). Although, ETO-1 demonstrated a reduced potency comparable to etomidate on $GABA_AR$ ($EC_{50}$: ETO-1 *vs*. ET: 11.47 *vs*. 4.55 μmol/L) and in mice ($ED_{50}$: ETO-1 *vs*. ET: 18.82 *vs*. 3.28 mg/kg), ETO-1 demonstrated a shorter recovery time of righting reflex at an equivalent dose ($2 \times ED_{50}$) (ETO-1 *vs*. ET: $98.0 \pm 9.2$ *vs*. $312.5 \pm 61.3$ s), consistent with our optimization goals. Based on these results, we selected ETO-1 as a lead compound for further structural optimization, expected to increase efficacy. In addition, ET-26 is a newly developed etomidate analogue with rapid onset, short-lasting general anesthesia, and is currently undergoing Phase III clinical trials (ChiCTR2400083014)[40,41]. Given its blockbuster potential in the global anesthetic market, this study employed ET-26 as a comparison (Fig. 1C). Since the *in vivo* activity of ET-26 was nearly 8 times lower than that of etomidate[42], we attempted to design derivatives based on the side chain structure of ET-26 in the hope of maintaining excellent properties while improving activity.

### 2.2. *Optimization of starting scaffold and candidate compound screening*

To create an etomidate derivative with rapid metabolism and high $GABA_AR$ affinity, we retained the carbonate group of ETO-1 that had been proved to be readily susceptible to hydrolase into the etomidate derivative[43]. Researches indicated an inverse correlation between the size of the side-chain alcohol substituent and CYP11B1-mediated side effects, alongside a positive correlation with $GABA_A$ receptor activity[44]. To enhance structural diversity, various different size alcohols were incorporated. Furthermore, to modulate metabolic clearance and identify optimal rates, diverse spacer groups were introduced[35]. This yielded a series of carbonate compounds (Fig. 1C). Building upon these findings, we designed and substituted the carbonate group with a *trans*-carboxylate ester moiety (stereochemical configuration opposite to that of the CPMM carboxylate) to comprehensively investigate the impact of this rational structural modification on pharmacological activity and the adverse effect profile. Several related derivatives were subsequently designed and synthesized to identify more potent analogs (Fig. 1C ester series). And the docking results also indicated that most of the compounds had higher affinity with $GABA_AR$ and lower affinity with CYP11B1, which providing theoretical support for the design (Supporting Information Tables S1 and S2).

The synthesis of the methyl carbonate series began with chloromethyl chloroformate (**1a**−**1c**) as the starting material (**1c** was synthesized according to the previously reported method[45]), which reacted with various alcohols (**2a**−**2m**) in the presence of pyridine to produce intermediates **3a**−**3w**. Etomidate acid (ET-COOH) was prepared from etomidate through hydrolysis under basic conditions. Intermediates **3a**−**3w** then underwent a nucleophilic substitution reaction with etomidate acid to produce compounds ETO-1−ETO-23 (Scheme 1, for rapid compound screening, diastereomeric mixtures were not further separated). Compounds ETO-24−ETO-27 obtained by raw materials **4a**−**d** reacted with ET-COOH as shown in Scheme 2. Similarly, **5a**−**5e** reacted with ET-COOH obtained compounds ETO-28−ETO-32 (Scheme 3).

Anesthetic drugs that undergo rapid metabolism through plasma esterase hydrolysis are widely used in clinical practice[46]. Therefore, using the synthesized compounds described above, we conducted a plasma decomposition assay *in vitro* to evaluate the metabolic rates of the synthesized compounds in rat plasma. The decomposition rates were calculated based on the detection and formation of etomidate acid released from the respective compounds. To conduct *in vitro* metabolism experiments, we screened the stability and solubility of these compounds. ETO-16−ETO-19, and ETO-23 were excluded due to their poor solubility (less than 1 mg/mL). As shown in Table 1, the ethyl carbonate series compounds rapidly decomposed, but their metabolic rate was slower than that of the methyl carbonate series compounds. Most of the compounds in the methyl carbonate series were rapidly decomposed within 20 min except for ETO-11. Among ester compounds, propyl carbonate compounds exhibited the slowest metabolic

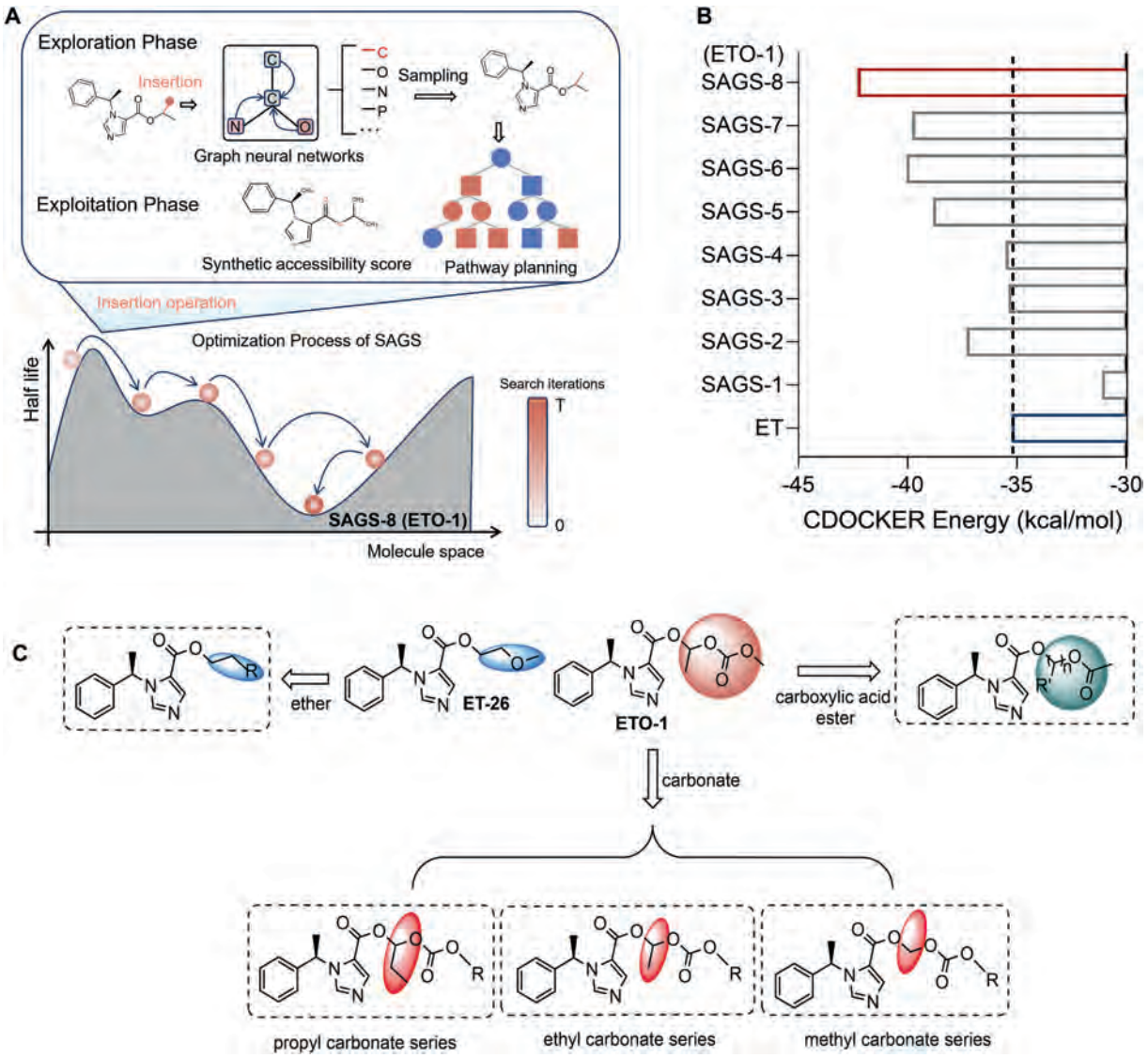


**Figure 1** Design of compounds. (A) Optimization process of SAGS to generate compounds with potential shorter half-lives than etomidate; (B) Molecular docking with $GABA_AR$ of SAGS-generated compounds showed that ETO-1 had a better docking score compared to etomidate; (C) Rational design of compounds. ET, etomidate; SAGS, simulated annealing for optimization of graphs and sequences.

rates. However, ether compounds showed virtually no metabolism in rat plasma within 60 min.

For all newly synthesized compounds, we found that the length and steric hindrance of etomidate derivatives affected the metabolic rate of compounds in rat plasma. Metabolites of compounds with a shorter side chain (*e.g.*, ETO-1, ETO-2, ETO-9, ETO-10, ETO-20 and ETO-21) were fully metabolized within 20 min. The metabolism of compounds with a large side chain space, such as ETO-11, was very slow ($t_{1/2} > 60$ min), and it further declined as the steric hindrance between the two ester groups increased. This was attributed to the excessive steric hindrance, which made it difficult for carboxylesterase to get close to the site of more readily occurring metabolism within the compound. In order to achieve rapid metabolism, compounds with $t_{1/2}$ greater than 60 min were excluded (ETO-6, ETO-8, ETO-11, and ETO-28−ETO-32).

For compounds screened through plasma metabolism, we conducted testing *in vitro* target activity. Based on the experimental solubility threshold (≥4 mg/mL) required for pharmacological evaluation, compounds ETO-5, ETO-7, ETO-13, and ETO-14 were excluded from activity screening due to insufficient solubility. Firstly, we evaluated the inhibitory activity of the newly synthesized compounds on the side effect target CYP11B1 (Supporting Information Fig. S2). Compared with etomidate and ET-26, the newly synthesized compounds all showed a significant increase in $IC_{50}$ values on CYP11B1, indicating a decrease in inhibitory effect on the adrenal cortex. It seems that the larger saturated alkyl group connected, the smaller inhibitory effect, manifested as $IC_{50}$ values ETO-1 < ETO-2 < ETO-3, ETO-9 < ETO-10, ETO-20 < ETO-21. When unsaturated groups are connected in the side chain, their inhibitory effect is lower, such as ETO-15. In carboxylic acid ester compounds, the presence of spacer carbon atoms can weaken the inhibitory effect on CYP11B1, manifested as $IC_{50}$ ETO-24 < ETO-25 and ETO-24 < ETO-26 (Table 2). Molecular docking shows that the 4-methoxy group in ETO-4 pushes the carbonyl oxygen away

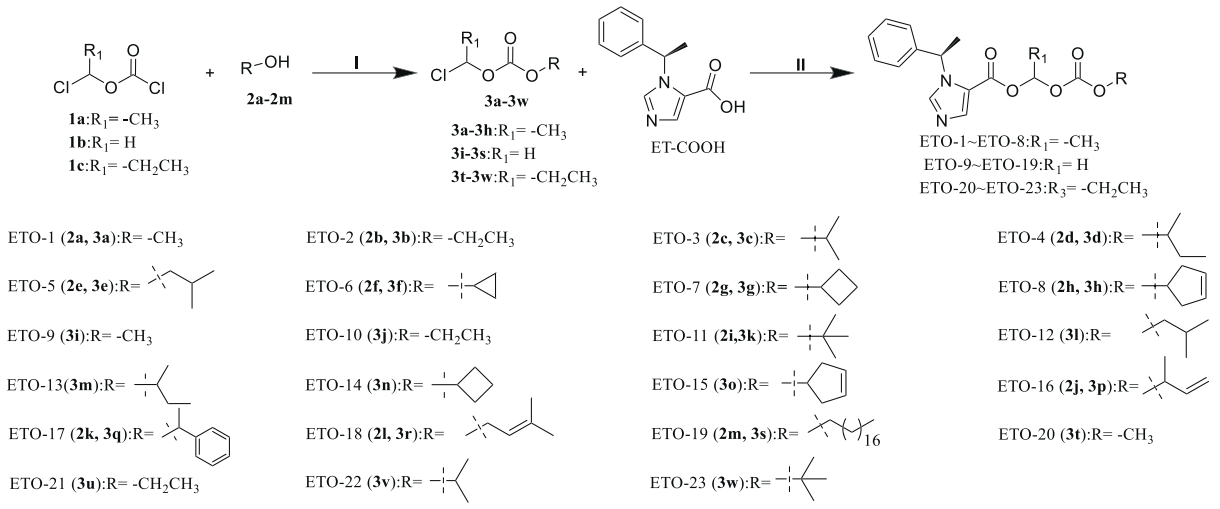


**Scheme 1** Synthetic route of carbonate series compounds. Conditions and reagents: (I) pyridine, DCM, rt, 2 h; (II) $K_2CO_3$, DMF, rt, 3 h.

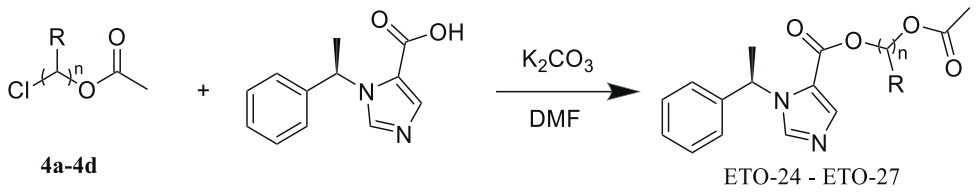


**Scheme 2** Synthetic route of carboxylic acid ester series compounds. Conditions and reagents: $K_2CO_3$, DMF, RT, overnight.

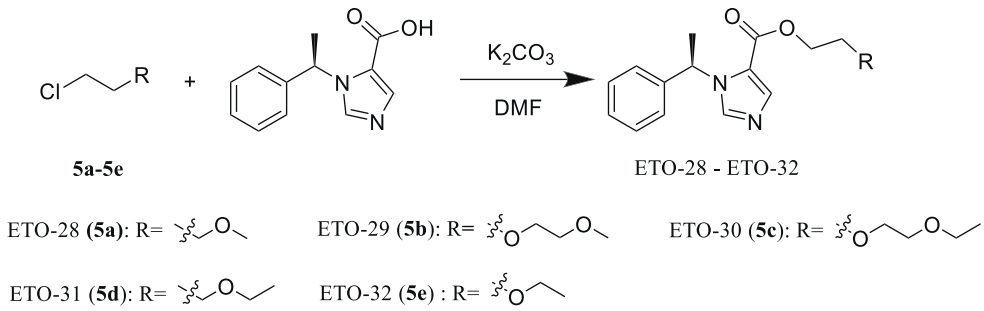


**Scheme 3** Synthetic route of ether series compounds. Conditions and reagents: $K_2CO_3$, DMF, RT, overnight.

from the heme iron (3.33 *vs* 2.48 Å in ET), abolishing iron coordination and weakening the interaction. Steric hindrance and the electron-donating effect of the methoxy group jointly reduce the carbonyl's nucleophilicity and conjugation with the aromatic ring, destroying the ligand-enzyme complex., rationalizing the observed loss of CYP11B1 inhibitory activity (Supporting Information Fig. S3).

Furthermore, we selected compounds with $IC_{50}$ greater than 50 nmol/L on CYP11B1 for *in vitro* $GABA_AR$ agonist activity testing. Results indicated that the activation strength on $GABA_AR$ by carboxylic acid ester compounds were weaker than that of carbonates, manifested as the maximum excitation current of ETO-25−ETO-27 being less than 800%, or even less than 200% (normalized to 3 μmol/L GABA). Moreover, compared to ET and ET-26, the excitatory activity is reduced ($EC_{50}$ greater than ET = 4.55 μmol/L, ET-26 = 27.98 μmol/L). In carbonate compounds, the excitatory activity of compounds with unsaturated groups attached seems to be higher than that of saturated alkanes, ($EC_{50}$: ETO-15 1.24 μmol/L < ETO-10 3.62 μmol/L), which may be due to stronger conjugation between the unsaturated groups at the molecular end and the receptor. Furthermore, when the side chains are connected to saturated alkanes, the excitatory activity of large alkyl groups is stronger than that of small alkyl groups ($EC_{50}$: ETO-4 < ETO-3 < ETO-1), which is consistent with previous studies[44].

Next, we evaluated the *in vivo* anesthetic effects of compounds obtained through *in vitro* screening. The loss of the righting reflex (LORR) was tested to determine the median effective dose ($ED_{50}$) of anesthesia for each compound. The $ED_{50}$ was calculated by the formula of up-and-down methods[42,47,48]. At the equivalent dose

**Table 1** Compounds screened by *in vitro* stability, solubility and plasma decomposition.

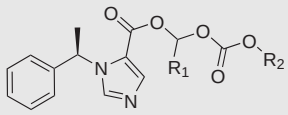

ETO-1~ETO-23

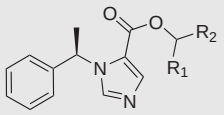

ET, ET-26, ETO-24~ETO-32

| Compd. | $R_1$ | $R_2$ | *In vitro* | | |
|---|---|---|---|---|---|
| | | | Stability[a] (%) | Solubility[b] (mg/mL) | $t_{1/2}$ (min) |
| Etomidate | H | $CH_3$ | 96.22 ± 0.19 | 41.51 ± 0.08 | >60 |
| ETO-1 | $CH_3$ | $CH_3$ | 94.11 ± 2.53 | 7.14 ± 0.09 | 6.0 |
| ETO-2 | $CH_3$ | $CH_2CH_3$ | 91.56 ± 1.75 | 4.78 ± 0.78 | 4.1 |
| ETO-3 | $CH_3$ | $CH(CH_3)_2$ | 92.95 ± 3.16 | 4.66 ± 0.59 | 12.6 |
| ETO-4 | $CH_3$ | $CH(CH_3)C_2H_5$ | 95.58 ± 2.47 | 6.70 ± 0.05 | <5 |
| ETO-5 | $CH_3$ | $CH_2CH(CH_3)_2$ | 88.15 ± 1.23 | 2.63 ± 0.30 | <5 |
| ETO-6 | $CH_3$ |  | 99.64 ± 0.21 | 3.25 ± 0.21 | >60 |
| ETO-7 | $CH_3$ |  | 93.17 ± 0.89 | 2.68 ± 0.86 | 26.7 |
| ETO-8 | $CH_3$ |  | 98.30 ± 0.62 | 4.16 ± 0.78 | >60 |
| ETO-9 | H | $CH_3$ | 92.28 ± 2.90 | 12.96 ± 5.60 | 5.2 |
| ETO-10 | H | $CH_2CH_3$ | 99.76 ± 0.51 | 13.86 ± 6.56 | 3.7 |
| ETO-11 | H | $C(CH_3)_3$ | 97.01 ± 2.33 | 0.85 ± 0.16 | >60 |
| ETO-12 | H | $CH_2CH(CH_3)_2$ | 96.76 ± 1.65 | 7.64 ± 1.06 | <5 |
| ETO-13 | H | $CH(CH_3)C_2H_5$ | 93.75 ± 1.80 | 2.49 ± 0.37 | 5.1 |
| ETO-14 | H |  | 97.52 ± 2.85 | 2.56 ± 0.39 | <5 |
| ETO-15 | H |  | 99.59 ± 0.35 | 6.23 ± 0.81 | <5 |
| ETO-16 | H |  | 94.39 ± 3.79 | 0.57 ± 0.01 | ND |
| ETO-17 | H |  | 93.35 ± 13.28 | 0.50 ± 0.01 | ND |
| ETO-18 | H |  | 56.57 ± 1.65 | ND | ND |
| ETO-19 | H |  | ND | ND | ND |
| ETO-20 | $CH_2CH_3$ | $CH_3$ | 97.70 ± 1.58 | 12.09 ± 1.99 | 6.3 |
| ETO-21 | $CH_2CH_3$ | $CH_2CH_3$ | 83.70 ± 11.23 | 7.85 ± 1.31 | 6.6 |
| ETO-22 | $CH_2CH_3$ | $CH(CH_3)_2$ | 94.84 ± 1.84 | 8.91 ± 1.24 | 29.5 |
| ETO-23 | $CH_2CH_3$ | $C(CH_3)_3$ | 73.83 ± 16.75 | 0.85 ± 0.54 | ND |
| ETO-24 | H |  | 99.39 ± 0.17 | 14.59 ± 0.07 | <5 |
| ETO-25 | H |  | 93.49 ± 0.46 | 7.20 ± 0.02 | <5 |
| ETO-26 | H |  | 99.42 ± 0.03 | 23.06 ± 0.01 | 8.8 |
| ETO-27 | $CH_3$ |  | 99.62 ± 1.45 | 19.50 ± 0.01 | 7.5 |
| ETO-28 | $CH_2CH_2OCH_3$ | H | 99.73 ± 1.07 | 18.17 ± 0.08 | >60 |
| ETO-29 | $CH_2O(CH_2)_2OCH_3$ | H | 99.24 ± 1.08 | 40.06 ± 0.31 | >60 |
| ETO-30 | $CH_2O(CH_2)_2OCH_2CH_3$ | H | 99.88 ± 0.11 | 46.56 ± 0.46 | >60 |
| ETO-31 | $CH_2CH_2OCH_2CH_3$ | H | 97.65 ± 1.04 | 10.11 ± 1.06 | >60 |
| ETO-32 | $CH_2OCH_2CH_3$ | H | 98.79 ± 0.28 | 17.98 ± 1.87 | >60 |
| ET-26 | $CH_2OCH_3$ | H | 95.66 ± 0.03 | 29.42 ± 0.99 | >60 |

[a]Stability assay: Dissolve the compound in PBS, let it stand at room temperature for 4 h, and measure the compound content through HPLC ($n = 3$).

$$\text{Remaining compound ratio (\%)} = \frac{4-\text{Hour compound peak area}/4-\text{Hour total area}}{0-\text{Hour compound peak area}/0\ \text{Hour total area}} \times 100.$$

[b]Solubility assay: Weigh 1 mg of the compound and dissolve it in 200 μL of methanol as the standard working solution. Dissolve the excess compound separately in a mixed solution of 20 μL PEG400 and 180 μL PBS to prepare a supersaturated solution. Measure the compound content in different solutions using HPLC.

$$\text{Concentration} = \frac{\text{Peak area of supersaturated solution}}{\text{Peak area of methanol solution}} \times \text{compound concentration of methanol solution.}$$

Data are presented as mean ± SD ($n = 3$); ND, no data.

**Table 2** Compounds screened by *in vitro* CYP11B1 inhibition, $GABA_AR$ agonist activity, and *in vivo* anesthetic evaluation.

| Compd. | *In vitro* | | | *In vivo* | | | |
|---|---|---|---|---|---|---|---|
| | CYP11B1 $IC_{50}$ (nmol/L) | $GABA_AR$ | | $ED_{50}$ (mg/kg) | $2 \times ED_{50}$ | | |
| | | $EC_{50}$ (μmol/L) | $A_{max}$ (%) | | Onset time (s) | RORR (s) | Time to walk (s) |
| Etomidate | 0.94 | 4.55 | 1143.13 | 3.28 | 1.3 ± 0.6 | 410.7 ± 48.2 | 452.2 ± 42.3 |
| ETO-1 | 2.92 | 11.47 | 1069.95 | 18.82 | 2.0 ± 0.0 | 98.0 ± 9.2 | 94.0 ± 14.0 |
| ETO-2 | 5.69 | – | | | | | |
| ETO-3 | 240.06 | 10.14 | 1448.33 | 11.38 | 5.7 ± 0.5 | 271.7 ± 6.2 | 77.0 ± 16.8 |
| ETO-4 | 173.90 | 1.79 | 1375.17 | 6.49 | 1.5 ± 0.6 | 157.1 ± 2.8 | 21.6 ± 1.8 |
| ETO-9 | 9.52 | – | | | | | |
| ETO-10 | 110.63 | 3.62 | 993.02 | 22.42 | 3.2 ± 1.5 | 67.3 ± 1.0 | 83.3 ± 29.0 |
| ETO-12 | 43.06 | – | | | | | |
| ETO-15 | 76.41 | 1.24 | 2098.15 | 20.98 | 2.7 ± 0.8 | 189.7 ± 17.9 | 94.3 ± 27.6 |
| ETO-20 | 34.95 | – | | | | | |
| ETO-21 | 81.10 | 5.63 | 1177.19 | 14.95 | 7.3 ± 3.5 | 123.2 ± 3.7 | 23.0 ± 6.6 |
| ETO-22 | 24.96 | – | | | | | |
| ETO-24 | 30.90 | – | | | | | |
| ETO-25 | 62.96 | 26.50 | 188.54 | 32.13 | 4.0 ± 1.1 | 128.5 ± 9.2 | 137.0 ± 11.3 |
| ETO-26 | 61.66 | 21.00 | 732.58 | 24.73 | 4.7 ± 1.5 | 109.0 ± 28.2 | 49.0 ± 15.7 |
| ETO-27 | 140.46 | 9.15 | 747.52 | 25.63 | 7.7 ± 3.0 | 145.3 ± 69.1 | 189.3 ± 48.1 |
| ET-26 | 31.9 | 27.98 | 1865.88 | 7.18 | 1.7 ± 0.6 | 312.5 ± 61.3 | 398.0 ± 102.8 |

$IC_{50}$, 50% inhibition concentration ($n = 2$); $EC_{50}$, 50% effective concentration ($n = 3$); $ED_{50}$, 50% effective dose ($n = 8$); RORR, recovery of righting reflex ($n = 8$); Data are presented as mean ± SD; ND, no data.
Note: "–" indicates that the compound has been excluded.

(100% effective dose, calculated as $2 \times ED_{50}$), the time of recovery of righting reflex (RORR) was evaluated. As shown in Tables 1 and 2, most compounds exhibiting more rapid metabolic rates necessitate higher doses in *in vivo* pharmacodynamic experiments. However, it is generally accepted that administering excessive doses increases safety risks[49]. Therefore, we selected compounds (ETO-3 and ETO-4) with anesthetic efficiency reduction within 4 times that of ET ($ED_{50} < 13$ mg/kg). Compounds exhibiting rapid plasma metabolism *in vitro* also demonstrated accelerated recovery from anesthesia *in vivo*. Since our goal was to minimize RORR time without significantly compromising the anesthesia potency of compounds, ETO-4 was selected (all compounds anesthetic evaluation *in vivo* was shown in Supporting Information Table S3).

*In vivo* potency assessments revealed that the compounds exhibited lower potency than ET. This reduced efficacy may be attributed to their significantly higher metabolic clearance rates compared to ET, particularly for ETO-4. Due to the fast metabolism rate, there were fewer prototype drugs that can cross the blood brain barrier (BBB) in a short period of time, requiring higher doses to achieve the same anesthetic effect. To further explain the influence of metabolic rate on the efficacy and duration of anesthesia. We conducted whole blood metabolic analyses of ET and ETO-4 respectively. The results showed that the metabolic rate of ETO-4 was much faster than that of ET (Supporting Information Fig. S4), which enabled ET to exist in its prototype for a longer time. Furthermore, the results of the plasma pharmacokinetic experiment of ETO-4 (Supporting Information Fig. S5 and Table S4) were consistent with the *in vitro* plasma metabolic rate. In the tissue distribution experiment (Supporting Information Figs. S6 and S7), the trend of plasma metabolism was consistent with that in the brain. When ETO-4 in the plasma decreased rapidly and significantly, ETO-4 in the brain also decreased, accordingly leading to awakening. However, ET in the plasma did not decrease rapidly, which gave them sufficient time to cross the blood–brain barrier to maintain anesthesia, which required more ETO-4 to reach the anesthetic dose. Among the selected compounds, ETO-4 possessed several advantages including a more rapid metabolism, a better anesthetic activity both *in vitro* and *in vivo*, lower inhibition of CYP11B1, and a shorter recovery time, which was identified as a candidate compound.

### *2.3. Molecular dynamics simulation and target verification of ETO-4*

For the candidate compound ETO-4, *in vitro* assays confirmed its high activity at the $GABA_AR$ ($EC_{50}$: ETO-4 *vs*. ET: 1.79 μmol/L *vs*. 4.55 μmol/L). The results of $GABA_A$ agonism activity from molecular dynamics (MD) simulations further validate the structural rationality. During the molecular dynamics simulations, the systems reached equilibrium after 80 ns, with root mean square deviation (RMSD) fluctuations remaining within 2.0 Å. After 150 ns, slight fluctuations were observed, with ETO-4 appearing more stable than ETO-1 and ET when complexed with the $GABA_AR$ (Supporting Information Fig. S8). The binding free energy calculations indicated that ETO-4 exhibited significantly lower binding free energy compared to ETO-1 and ET. Additionally, ETO-4 demonstrated stronger Coulombic and van der Waals interactions, along with a notable increase in polar solvation energy, which was associated with differences in binding modes (Supporting Information Table S5). Both ET (Fig. 2A) and ETO-1 (Fig. 2B) adopt an elongated, rod-like conformation between the $\alpha 1\beta 2$ subunits of the $GABA_AR$, whereas ETO-4 bound in a U-shaped conformation within the pocket formed by the subunits (Fig. 2C). Notably, the nitrogen atom of the imidazole ring in the core structure of ETO-4 formed a hydrogen bond with the residue Arg269. By extending the structure starting from the core of ET,

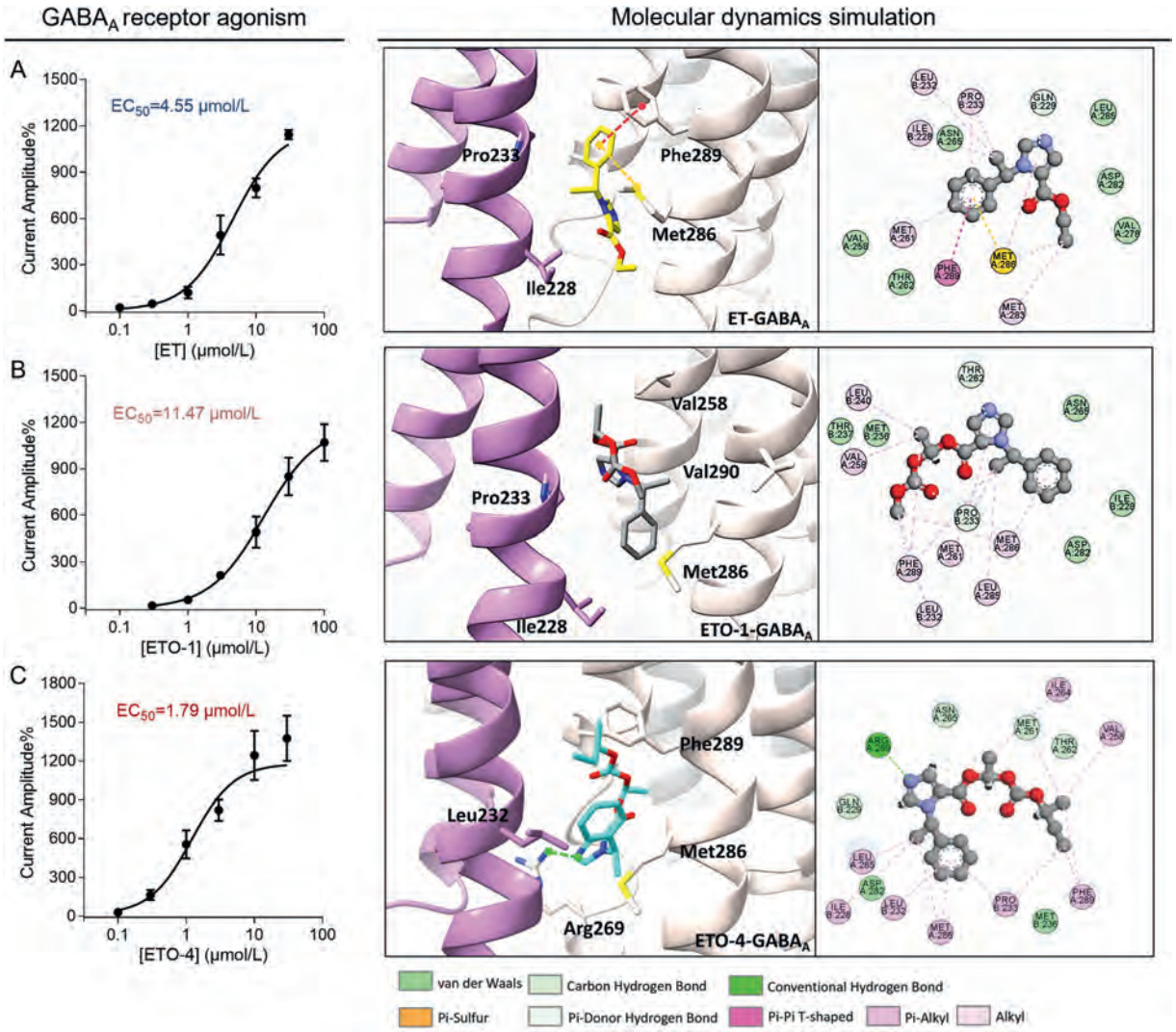


**Figure 2** GABA$_A$ agonism test and molecular dynamics simulation. The GABA$_A$ receptor agonism and molecular dynamics simulation of ET (A), ETO-1 (B), and ETO-4 (C). Abbreviation in figures: GABA$_A$ receptors, gamma-aminobutyric acid type A receptors; ET, etomidate; EC$_{50}$, median effective concentration.

ETO-4 increased the contact area between the ligand and receptor, which generally led to more interactions. The introduction of the hydrocarbon hydrophobic group at the terminal of ETO-4 significantly enhanced interactions with hydrophobic amino acid residues, such as Phe289 (Supporting Information Table S6), located at the mouth of the subunit pocket, potentially improving its solubility in lipid bilayers.

To further validate the target of ETO-4 exerting anesthetic effects, we used GABA$_A$R antagonist for pretreatment. The mice were pretreated with bicuculline[50,51] (a competitive antagonist of GABA$_A$R) and picrotoxinin[52] (a noncompetitive antagonist of GABA$_A$R). ETO-4 (2 × ED$_{50}$) was given 1 min after that because we confirmed in preliminary experiments that convulsions induced by these drugs occur within 3 min after injection. The results indicated that when mice were pretreated with bicuculline or picrotoxinin, the RORR time was significantly shortened in a dose-dependent manner, while the epilepsy score increased in a dose-dependent manner (Fig. 3). These results demonstrated that ETO-4 was anesthetic sedatives targeted on GABA$_A$ receptors.

### 2.4. *Pharmacodynamic activity and safety evaluation of ETO-4*

Then, we evaluated the pharmacodynamic activity and safety profiles for inducing and maintaining general anesthesia during surgery *in vivo*. Initially, to determine appropriate doses for general anesthesia, we evaluated the ED$_{50}$ (ETO-4 *vs.* ET: 4.52 mg/kg *vs.* 2.38 mg/kg) in rats using the previously described up-and-down methods. Next, we conducted a continuous infusion experiment through the tail vein of rats to simulate clinical application. ET and ETO-4 were administered *via* continuous infusion to maintain LORR of rats for 30 min. Induction doses were 2 × ED$_{50}$ of rats for each compound, and maintenance doses were the minimum required to maintain LORR in rats, which were determined by preliminary experiments. During the process, the anesthetic depth was evaluated by the electroencephalogram (EEG), the heart rate, electrocardiogram (ECG), respiratory rate and any related adverse events were recorded as well to assess the impact on the heart and breathing. The RORR time and time to walk following cessation of the continuous infusion was recorded for assessing anesthesia recovery.

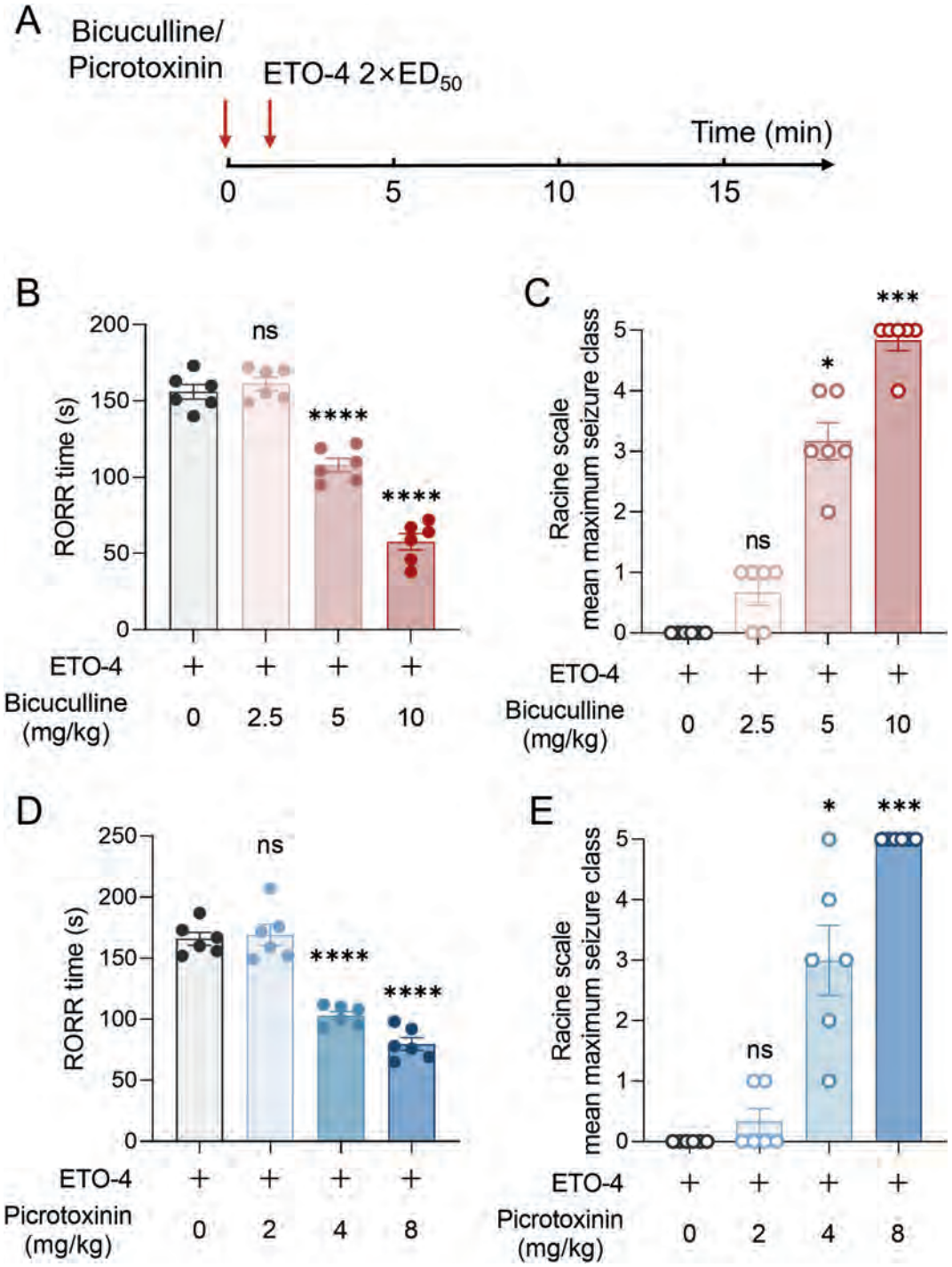


**Figure 3** Pre-treatment with bicuculline and pricotoxinin inhibits the sedative effect of ETO-4. (A) ETO-4 was injected 1 min after bicuculline or pricotoxinin. (B, D) The RORR time was significantly shortened in a dose-dependent manner with pre-treatment of bicuculline or pricotoxinin ($n = 6$). (C, E) The epilepsy score increased in a dose-dependent manner with pre-treatment of bicuculline or pricotoxinin ($n = 6$). Statistical analysis was performed using one-way ANOVA followed by Tukey's *post hoc* test. Data are presented as mean ± SEM. ns $P > 0.05$, *$P < 0.05$, ***$P < 0.001$, and ****$P < 0.0001$. Abbreviation in figures: RORR, recovery of righting reflex.

Results indicated that the RORR time of ETO-4 was significantly shorter than that of ET (ETO-4 *vs*. ET: 163.8 ± 19.0 s *vs*. 441.7 ± 25.8 s, $P < 0.0001$) (Fig. 4A). Also, time to walk was significantly faster in the ETO-4 group compared to the ET group (ETO-4 *vs*. ET: 230.7 ± 32.8 s *vs*. 549.2 ± 44.9 s, $P < 0.001$) (Fig. 4B). Meanwhile, EEG results showed a trend towards a shift from high-frequency to low-frequency waveforms as anesthesia deepened following the administration of anesthetics. After administration of ET, an increase in low-frequency waves was observed, indicating that the animals entered the maintenance phase of anesthesia[53]. However, after administration of an equivalent dose of ETO-4, burst suppression (BS) appeared in

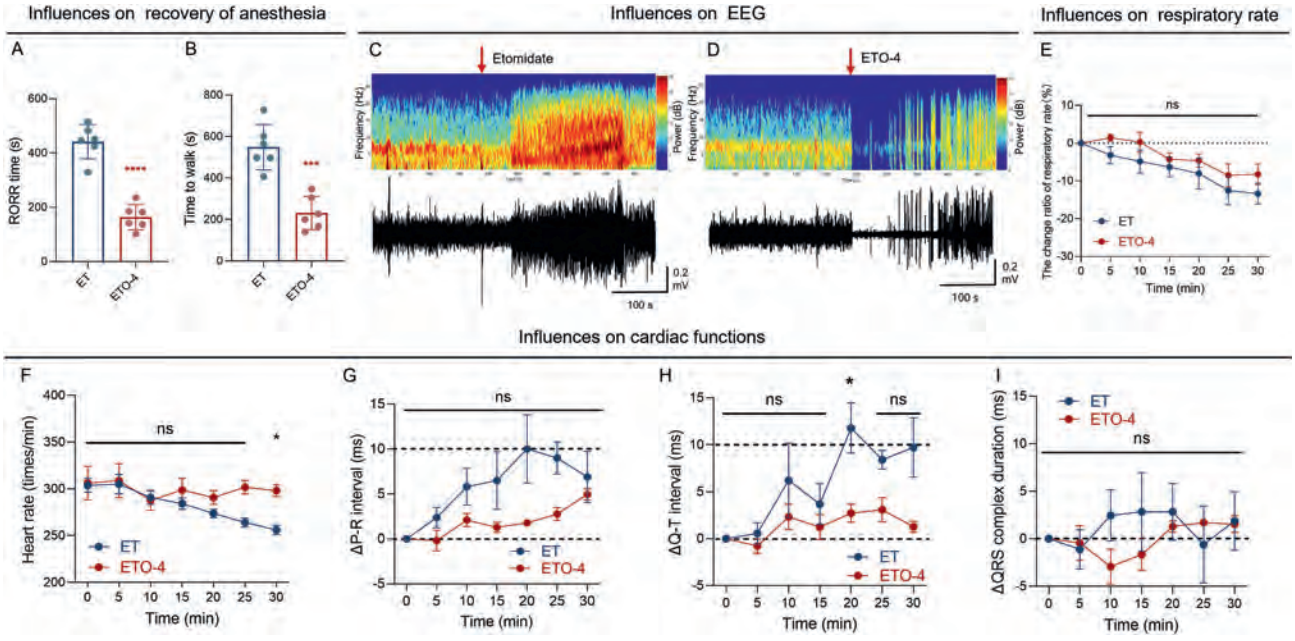


**Figure 4** Anesthetic efficacy and safety evaluation during continuous administration of etomidate and ETO-4. (A, B) The recovery time of righting reflex and time to walk of rats after continuous infusion of ET and ETO-4 ($n = 6$). (C, D) The EEG of rats after administration of ET and ETO-4 ($n = 3$). (E) The influence on respiratory rate of rats during continuous infusion of ET and ETO-4 ($n = 3$). (F) The influence on heart rate of rats during continuous infusion of ET and ETO-4 ($n = 3$). (G−I) The change of P-R interval, Q−T interval and QRS complex duration of rats during continuous infusion of ET and ETO-4 ($n = 3$). Statistical analysis was performed using two-tailed paired Student's *t*-tests or two-way ANOVA followed by Tukey's *post hoc* tests. Data are presented as mean ± SEM. ns $P > 0.05$, $^{*}P < 0.05$, $^{***}P < 0.001$, and $^{****}P < 0.0001$. Abbreviation in figures: ET, etomidate; RORR, recovery of righting reflex; EEG, electrocardiogram.

EEG, characterized by alternating high-frequency burst waves and low-frequency suppression waves[54], followed by a predominantly low-frequency anesthetic state. It is worth noting that such phenomenon was common in severe brain injury, hypoxic encephalopathy, or overly deep anesthesia in clinical practice. To further determine that ETO-4 merely increases the depth of anesthesia rather than causes neurological lesions, we conducted the CCK8 experiment to evaluate the brain nerve cells by using this compound. The results are shown in the Supporting Information Fig. S9 at the concentration of 50 μmol/L, there was almost no cytotoxicity to SH-SY5Y and N2a cells. The burst suppression rate also returned to normal as the mice woke up (Supporting Information Fig. S10) which indicates that this compound has no effect on brain waves in the waking state. In addition, no related neurological lesions were found in the behavioral assessment of mice and rats after their recovery from anesthesia in the later stage. Therefore, the EEG results demonstrate that ETO-4, at an equivalent dose, induces a deeper state of anesthesia (Fig. 4C and D). Furthermore, we did not observe any characteristics related to epileptic waves in the electroencephalogram and no symptoms of

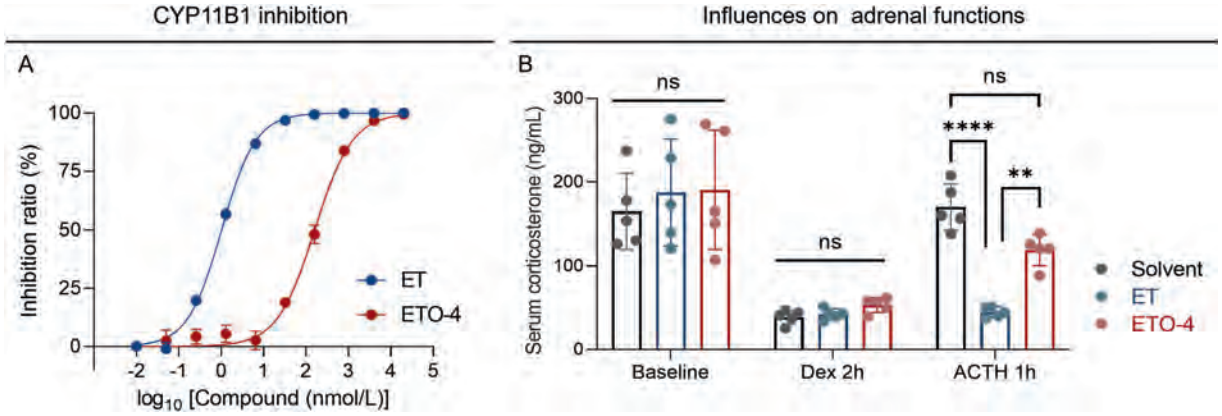


**Figure 5** The inhibition of adrenal function by ETO-4 *in vitro* and *in vivo*. (A) CYP11B1 inhibition ratio of ET and ETO-4 ($n = 2$). (B) The corticosterone concentrations of rats administrated ET and ETO-4 ($n = 5$). Statistical analysis was performed using two-tailed paired Student's *t*-test or one-way ANOVA followed by Tukey's *post hoc* tests. Data are presented as mean ± SEM. ns $P > 0.05$, $^{**}P < 0.01$, and $^{****}P < 0.0001$. Abbreviations in figures: ET, etomidate; Dex, dexamethasone; ACTH, Adrenocorticotropic hormone.

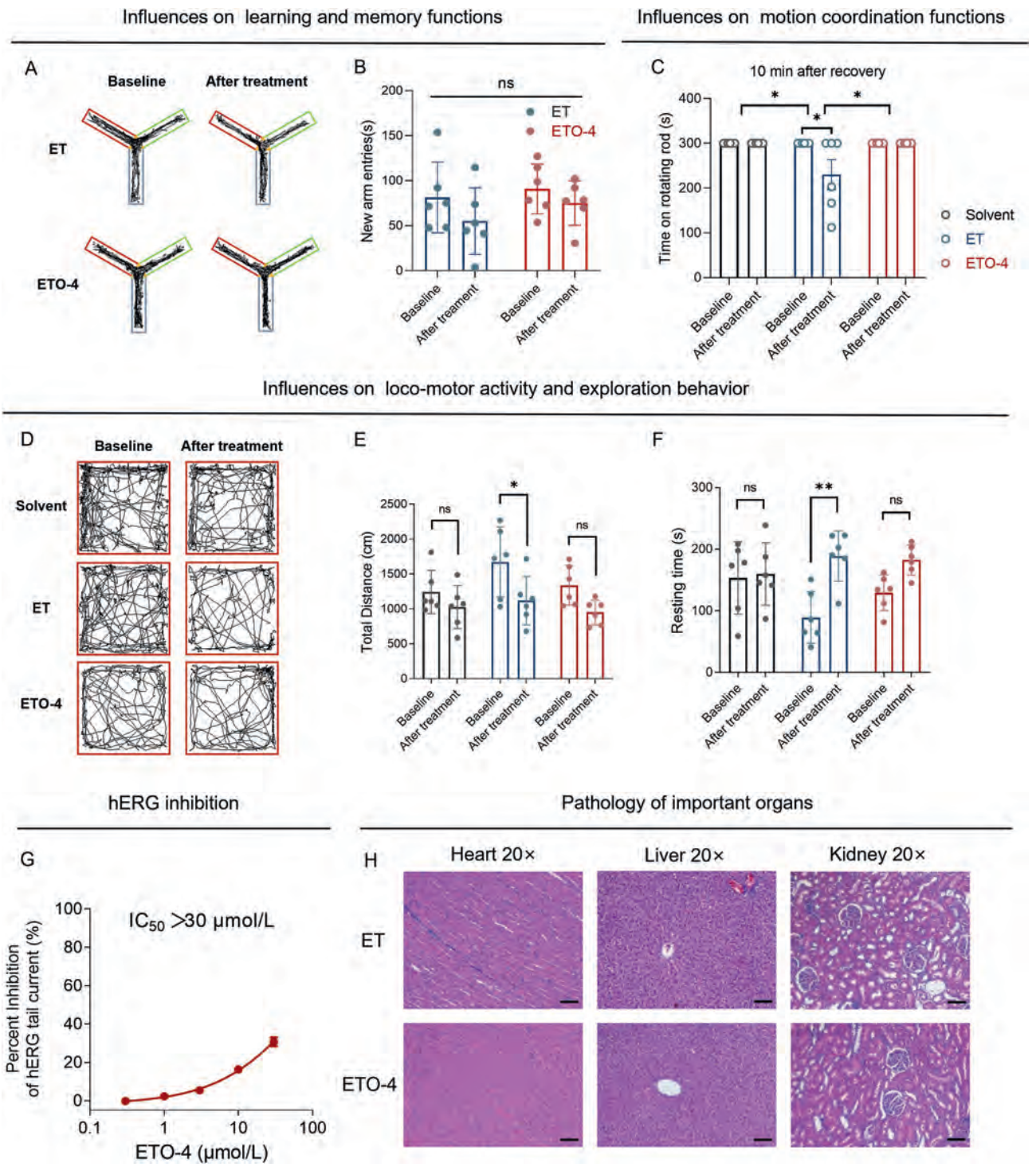


**Figure 6** Evaluation of the safety profiles of ETO-4. (A, B) The influence of ET and ETO-4 on learning and memory functions by Y-maze tests, ($n = 6$). (C) The influence of ET and ETO-4 on motion coordination functions by rotarod tests, ($n = 6$). (D−F) The influence of ET and ETO-4 on loco-motor activity and exploration behavior by open field tests, ($n = 6$). (G) Evaluation of hERG inhibitory activity of ETO-4. (H) Evaluation of the pathology of important organs after administration. Statistical analysis was performed using one-way ANOVA followed by Tukey's *post hoc* test. Data are presented as mean ± SEM. ns $P > 0.05$, $^{*}P < 0.05$, and $^{**}P < 0.01$. Scale bar = 50 μm (20 × ). Abbreviations in figures: ET, etomidate; $IC_{50}$, median inhibition concentration; hERG, the human Ether-à-go-go-Related Gene.

epilepsy were observed after the administration, which suggests that this compound does not cause epilepsy related neurotoxicity. Besides, fluctuations of respiratory rate and heart rate were less pronounced during continuous ETO-4 infusion than during continuous ET infusion (Fig. 4E and F). Furthermore, the ECG indicated that ETO-4 has less effect than ET on the variation in P−R interval, Q−T interval, and QRS complex duration (Fig. 4G−I). Thus, ETO-4 showed better anesthetic activity, and a faster

recovery time *in vivo* compared with ET, consistent with the results of plasma decomposition *in vitro* and molecular simulations.

The observed excellent efficacy associated with ETO-4 prompted a thorough investigation into its broader safety profiles. Initially, we calculated therapeutic index (TI = $LD_{50}/ED_{50}$) of ETO-4 *in vivo*, which was almost twice that of ET, indicating better safety (ETO-4 *vs.* ET: 38.83 *vs*. 21.13), the dose-response curves of the two compounds were shown in Supporting Information Fig. S11, which indicated that ETO-4 has a wider therapeutic window. Then, the inhibitory effect of ETO-4 on adrenal cortical function was assessed. The *in vitro* inhibition of human CYP11B1 assay result showed that ETO-4 significantly reduced inhibition of CYP11B1, which had a lower inhibition of CYP11B1 than ET ($IC_{50}$: ETO-4 *vs.* ET = 173.90 *vs.* 0.94 nmol/L, Fig. 5A). Next, we used an adrenocorticotropic hormone ($ACTH_{1-24}$) stimulation experiment in rats to assess the *in vivo* effects of ETO-4 on adrenal function[27]. To reduce endogenous cortisol production, we pre-administrated dexamethasone (Dex). Solvent, ET, and ETO-4 were administered 2 h later, and $ACTH_{1-24}$ was administered 15 min after that. The serum was separated from the venous blood 1 h later, and the serum cortisol concentration was detected using a cortisol enzyme-linked immunosorbent assay kit. The concentration of serum corticosterone in the rats is presented in Fig. 4B. Dexamethasone suppressed the concentration of corticosterone to 53.25 ± 4.01 ng/mL in the ETO-4 group, to 42.18 ± 3.01 ng/mL in the ET group, and to 38.86 ± 3.70 ng/mL in the solvent group, with no significant difference among the groups ($P = 0.730$). One hour after $ACTH_{1-24}$ administration, the rats that had received ETO-4 had higher corticosterone concentrations than the rats that had received ET (ETO-4 *vs.* ET: 119.20 ± 8.37 *vs*. 44.69 ± 2.82 ng/mL, $P < 0.05$), which showed significant improvement compared with the ET group (Fig. 5B). These results suggest that ETO-4 had a weaker inhibitory effect on the adrenal cortical function and accelerated the recovery of corticosterone level.

In addition, we also compared the effects of ETO-4 and ET on learning and memory functions, motor coordination, loco-motor activity and exploration behavior in mice. The Y maze test suggested that neither ET nor ETO-4 affected the learning and memory functions of mice (Fig. 6A and B). The rotarod test indicated that, compared to ET, ETO-4 allowed for a faster recovery of motor coordination ability following general anesthesia (Fig. 6C). The open field test suggested that, relative to ET, ETO-4 enabled a faster recovery of loco-motor activity after anesthesia, particularly in terms of total distance and resting time (Fig. 6D–F).

Furthermore, a systematic approach was employed to evaluate biochemical indicators and potential organ damage. The $IC_{50}$ of ETO-4 for hEGR (the human Ether-à-go-go-Related Gene) channel inhibition exceeded 30 μmol/L (Fig. 6G), suggesting no hERG inhibition. Additionally, the biochemical indicators demonstrated that no significant differences were noted in key biochemical parameters such as alanine aminotransferase (ALT), aspartate aminotransferase (AST), creatinine (CREA), urea nitrogen (UREA), α-hydroxybutyrate dehydrogenase (α-HBDH), and lactic dehydrogenase (LDH) levels between solvent and ETO-4 groups. While there were slight elevations in ALT, AST, UREA and LDH levels in the ET group (Supporting Information Fig. S12). Furthermore, to assess any potential organ damage attributable to ETO-4, we conducted histopathological examinations. Harris's hematoxylin and eosin (H&E) staining was performed on major organs, including liver, heart, and kidney of rats. The histological analysis revealed no significant morphological alterations in these organs (Fig. 6H), suggesting the absence of organ-specific toxicity from ETO-4. Moreover, the impact of ETO-4 on drug metabolism was assessed, focusing on four major cytochrome P450 (CYP450) subtypes: CYP1A2, CYP2C8, CYP2D6, CYP2E1. At a concentration of 10 μmol/L, ETO-4 did not exhibit noticeable inhibition on these enzymes (Supporting Information Table S7). Collectively, these results affirm that ETO-4 are associated with higher safety profiles, marking it as a promising candidate in clinical applications.

## 3. Conclusions

In this study, we leveraged SAGS to identify a rapidly metabolized etomidate lead compound, ETO-1, and subsequently introduced a series of etomidate derivatives with improved metabolic profiles. Comprehensive *in vitro* and *in vivo* assessments allowed us to characterize both the metabolic kinetics and the anesthetic properties of these derivatives. Among these derivatives, ETO-4 emerged as particularly promising, exhibiting a significantly faster metabolic clearance than the parent compound etomidate, without compromising anesthetic efficacy, which $GABA_A$ agonist activity had significantly improved. And the molecular dynamics simulation experiment explained the rationality of the results. Notably, ETO-4 demonstrated a favorable therapeutic index, exerted minimal hemodynamic impacts, and induced more rapid postoperative recovery. Its reduced suppression of adrenal cortical function, combined with the absence of deleterious effects on motor coordination, cognition, and organ integrity, underscores its improved safety and tolerability profiles.

These findings not only highlight ETO-4 as a candidate with strong translational potential but also reinforce the underlying rationale that accelerating drug metabolism can effectively mitigate prolonged postoperative side effects—an approach that circumvents the longstanding challenge of modulating receptor-level specificity alone. By tightly integrating experimental design with clinically informed endpoints, this work exemplifies a research paradigm that bridges the gap between bench discoveries and bedside applications. Furthermore, the utilization of clinically relevant data to guide molecular optimization and subsequent preclinical evaluations provides a template for the development of next-generation anesthetics and related therapeutics.

## 4. Experimental

### *4.1. Methods of AI screening*

#### *4.1.1. A detailed description of the SAGS algorithm*

The molecule optimization algorithm SAGS (Simulated Annealing for Graphs and Sequences) is a sophisticated computational strategy for the targeted optimization of molecular graph structures. It belongs to a class of Markov Chain Monte Carlo (MCMC) methods that strategically combines the global search capabilities of Simulated Annealing (SA) with the predictive power of modern deep learning, specifically a pre-trained Graph Neural Network (GNN), to efficiently navigate the vast and complex chemical space. The primary objective of SAGS is to iteratively refine an initial molecule to maximize a specific objective function, which typically quantifies a desired molecular property such as drug binding affinity, synthetic accessibility, or solubility.

As shown in Algorithm 1, the algorithm proceeds through a sequence of iterations, meticulously refining the molecular structure (Step 1). The process begins with the input of a seed molecule $x_0$, which serves as the starting point for the optimization trajectory. In step 2, the temperature $t$ for the current iteration is calculated in a form of a linear cooling schedule, a hallmark of simulated annealing. Initially, the temperature $T_{\text{init}}$ is high, promoting extensive exploration of the chemical space by allowing the algorithm to accept molecular changes even if they lead to a worse objective value. As the iteration index approaches the total number of iterations $K$, the temperature asymptotically approaches zero. This systematic cooling forces the algorithm to transition from a broad, exploratory search to a more focused, exploitative refinement, increasingly favoring only those modifications that yield an improvement in the objective function. This carefully calibrated schedule is critical for avoiding convergence to local optima.

At the heart of each iteration is the proposal of a new candidate molecule $x'$. This is a two-step process: (1) Random Selection (Step 3): The algorithm first randomly selects an atomic position within the current molecule and a modification operation (changing an atom type, adding a bond, deleting an atom). This stochastic selection ensures the algorithm can explore a diverse set of structural changes. (2) Informed Generation (Step 4): Instead of applying the modification blindly, the algorithm employs a pre-trained GNN to sample the candidate molecule. The GNN, trained on a large corpus of chemical data, acts as an intelligent "candidate molecule generator". It leverages the intrinsic graph structure of the molecule (atoms as nodes, bonds as edges) to propose a chemically plausible and context-aware modification at the chosen site. This integration of a GNN dramatically increases the efficiency of the search by biasing the proposal distribution towards regions of chemical space that are both valid and likely to contain high-value molecules, effectively reducing the vastness of the search space.

Following the generation of the candidate $x'$, the algorithm must decide whether to adopt it as the new state (Step 5). This decision is not deterministic but probabilistic, using the acceptance probability, $p(\text{accept}|x', x_k, t)$, which is given by Eq. (1):

$$p(\text{accept}|x', x_k, t) = \min\left(1, e^{\frac{f(x')-f(x_k)}{t}}\right) \tag{1}$$

If the new molecule $x'$ has a higher score ($f(x') > f(x_k)$), the exponent is positive and the probability is 1, meaning the move is always accepted. If it has a lower score, the probability is determined by the exponent of the normalized difference $\frac{f(x')-f(x_k)}{t}$. A higher temperature $t$ makes accepting a worse solution more likely, facilitating exploration.

This probabilistic decision is executed in Steps 6 and 7. A random number is drawn and compared to the calculated probability. If the number is below the threshold, the candidate is accepted. Otherwise, it is rejected, and the chain remains at the previous state. Rejection is a crucial mechanism, preventing the algorithm from descending into unfavorable regions of the molecular landscape.

After the completion of all iterations, the algorithm does not simply return the final molecule. Instead, it performs a final optimization step (Step 9): it returns the molecule that achieved the highest objective function value $f(x_k)$ encountered throughout the entire search history. This best-so-far archival ensures that the algorithm's output is not undermined by any unfortunate downhill moves accepted in the final, low-temperature steps.

In summary, the SAGS algorithm represents a powerful synergy between traditional stochastic optimization and cutting-edge deep learning. It harnesses the exploratory strength of simulated annealing, tempered by a defined cooling schedule, and directs its search intelligently through the use of a GNN-based proposal mechanism. This makes it particularly well-suited for complex molecular optimization problems where the search space is intractably large and the objective function is expensive to evaluate, offering a robust and efficient path towards the discovery of novel molecules with optimized properties.

**Algorithm 1.** The SAGS algorithm pseudocode. $K$ stands for the iteration number and $t$ is the temperature that controls the acceptance probability. $T_{\text{init}}$ represents the initial temperature and $C$ represents the cooling coefficient. $x_k$ is the edited molecule at step $k$ and $x^*$ is the optimal molecule generated by SAGS.

Input: The given molecule $x_0$ to be optimized

1: for $k \in \{1, 2, \cdots, K\}$ do
2: $t = \max\{T_{\text{init}} - C \cdot k, 0\}$
3: Randomly select a modification position and a modification operation
4: Sample a candidate molecule $x'$ using the pre-trained GNN
5: Compute $p(\text{accept}|x', x_k, t)$
6: Accept: $x_{k+1} = x'$ with the probability $p(\text{accept}|x', x_k, t)$
7: Otherwise: $x_{k+1} = x_k$
8: end for
9: return $x^* = \underset{x_k}{\text{argmax}} f(x_k)$

#### 4.1.2. *Implementation details of SAGS*

The initial temperature $T_{\text{init}}$ of SAGS was 0.01 and the cooling coefficient was set to $3 \times 10^{-6}$. The maximum number of searching iterations $K$ was set to 200. For the training of random forest regressor, we collected 5467 molecules and the corresponding half-life values from related studies[55,56] as the training dataset. The random forest regressor had 100 estimators and the cost criterion is the mean square error. The inputs of the regressor were the chemical features (including number of rotatable bonds, solubility, molecule weights, etc.) of a given molecule and the output of the regressor was the corresponding half-life value.

We adopted the pre-trained GNN (called candidate molecule generator) in[56] as the generative model in SAGS to propose editing atoms. The candidate molecule generator is composed of a stack of 5 identical layers; each layer performs a shared message passing operation for 3 times recurrently to enable larger receptive fields with less parameters. It is pre-trained on a largescale dataset that contains 11 million molecules from ZINC and ChEMBL datasets. To preserve the diversity, the filtered molecules from ZINC cover a wide range of molecular weight ($\geq$200 Da) and Log$P$ ($\geq$1). During the searching process of SAGS, we omitted the molecule candidates whose similarity was lower than 0.8 to preserve the structural function of etomidate.

#### 4.1.3. *Computational experiments of the SAGS algorithm*

We followed Jin et al.'s protocol[57] and took the molecular solubility (measured by the penalized Log$P$ property) as an example to

evaluate the performance of SAGS. Specifically, we collected 800 molecules in ZINC250K[58] with the lowest scores as the starting molecules to be optimized. We compared SAGS with three competing baselines, including the genetic algorithm (GA), the molecule swarm optimization (MSO)[59], and the junction-tree variational auto-encoder (JT-VAE)[57]. The improvements of the optimized molecules and the success rates are reported in Table 3. We observed that the SAGS algorithm largely outperformed the other molecule optimization algorithms in terms of the improvement scale on the penalized Log*P* property, indicating the powerful optimization capacity of SAGS. We have also tested the predictive performance of the random forest model (RF), which serve as part of the objective function of SAGS. The mean square error between the predicted half-life values and the ground truth is 0.23 and the mean absolute error is 0.15, which is a reasonable performance for RF to indicate the quality of a molecule candidate.

### *4.2. Chemistry*

All materials and reagents were commercially available and used without further purification. Reactions were monitored by thin-layer chromatography (TLC) with silica gel GF254 (0.25 mm, Qingdao Ocean Chemical, Ltd., China). Column chromatography (CC) was performed on a silica gel (200−300 mesh, Qingdao Ocean Chemical, Ltd., China). The mass spectra were recorded on an Thermo Q-Exactive Plus LC−MS mass spectrometer (Thermo Company, USA). $^{1}$H and $^{13}$C NMR spectra were recorded on Bruker AVANCE NEO spectrometer (Bruker Company, Germany) with TopSpin 4.3.0 software for both routine and advanced NMR acquisition and analysis, using TMS as an internal standard and $CDCl_3$ as solvent at 25 °C. In the NMR tabulation, s indicates singlet; d, doublet; t, triplet; q, quartet, and m, multiplet. Chemical shifts are expressed in ppm ($\delta$). High-performance liquid chromatography (HPLC) analyses were performed on a Shimadzu HPLC system in a reverse mode with a MLtimate XB-C18 column (4.6 mm × 250 mm, 5 μm) using a water/methanol (each with 0.1 % (*v*/*v*) trifluoroacetic acid) gradient at a flow rate at 1.0 mL/min. The purities of all final compounds were >95% by HPLC.

#### *4.2.1. General procedure for preparation of compounds ETO-1−ETO-23 (with ETO-1 as an example)*

To a solution of etomidate (10 g in methanol (50 mL)), 50 mL of 2 mol/L NaOH aqueous solution was added. Then the reaction was stirred at room temperature overnight. The reaction progress was monitored by TLC. After the reaction is completed, the organic solvent was removed by distilling under reduced pressure. The reaction solution was extracted with dichloromethane. After the extraction, the organic phases were collected, dried with anhydrous $Na_2SO_4$, filtered, concentrated under reduced pressure, and dried to obtain etomidate acid (ET-COOH, 9.1 g, 96.12%), as white powder.

To a 200 mL round-bottomed flask, methanol (1.49 g, 46.53 mmol, 1.2 eq.), dichloromethane (100 mL) was added, then the chloroethyl chloroformate (**2a**, 5.0 g, 38.78 mmol, 1 eq.) was added dropwise while the round-bottomed flask in an ice water bath. Pyridine (4.60 g, 58.17 mmol, 1.5 eq.) was slowly added dropwise, and the reaction was stirred at room temperature for 2 h. After the reaction was completed, the organic solvent was removed under reduced pressure to obtain white pyridinium salt. Use 2 mol/L HCl to dissolve the pyridinium salt. The solution was extracted with ethyl acetate. The organic phase was collected and dried, then concentrated under reduced pressure to obtain the crude product of compound **3a**, $^{1}$H NMR (400 MHz, Chloroform-*d* ) $\delta$ 6.44 (q, $J$ = 5.8 Hz, 1H), 3.86 (s, 3H), 1.83 (d, $J$ = 5.8 Hz, 3H), which is directly used in the next step reaction.

*N*,*N*-Dimethylformamide (50 mL), etomidate acid (2.0 g, 9.25 mmol, 1.0 eq.) and anhydrous $K_2CO_3$ (1.92 g, 13.87 mmol, 1.5 eq.) were added into a 200 mL round-bottomed flask. Then compound **3a** (1.38 g, 12.10 mmol, 1.5 eq.) was added after 10−20 min, and the reaction was stirred for 3 h at room temperature. The reaction was detected by TLC. After the reaction was completed, the organic solvent in the reaction solution was distilled off under reduced pressure. After extracting water and ethyl acetate, the organic phase was collected and dried with add anhydrous $Na_2SO_4$, then the solution was concentrated under reduced pressure to obtain crude target compound. The crude product was purified by column chromatography to obtain compound ETO-1 (0.92 g, 32.8%, light yellow oil).

*(R)-1-(1-Phenylethyl)-1H-imidazole-5-carboxylic acid (ET-COOH).* Yield, 96.12%; $^{1}$H NMR (400 MHz, $CDCl_3$) $\delta$ 7.88 (d, $J$ = 1.0 Hz, 1H), 7.76 (t, $J$ = 2.6 Hz, 1H), 7.38−7.28 (m, 3H), 7.20 (dd, $J$ = 5.4, 3.6 Hz, 2H), 6.40 (q, $J$ = 7.2 Hz, 1H), 5.94 (d, $J$ = 5.8 Hz, 1H), 5.86 (d, $J$ = 5.8 Hz, 1H), 3.84 (s, 3H), 1.86 (d, $J$ = 7.2 Hz, 3H) ppm. $^{13}$C NMR (100 MHz, $CDCl_3$) $\delta$ 158.31, 154.51, 140.80, 140.65, 139.90, 128.91, 128.87, 128.16, 126.32, 121.13, 81.61, 55.62, 55.34, 22.18 ppm. HRMS Calcd. for $C_{12}H_{13}N_2O_2$ $[M+H]^+$ 217.0977. Found: 217.0971.

*(R,S)-1-((Methoxycarbonyl)oxy)ethyl 1-((R)-1-phenylethyl)-1H-imidazole-5-carboxylate (ETO-1).* Yield, 38.25%; $^{1}$H NMR (400 MHz, $CDCl_3$) $\delta$ 7.83 (t, $J$ = 1.2 Hz, 1H), 7.39−7.28 (m, 3H), 7.25−7.21 (m, 1H), 7.20−7.16 (m, 1H), 6.93 (qd, $J$ = 5.4, 3.2 Hz, 1H), 6.32 (m, 1H), 3.80 (d, $J$ = 8.8 Hz, 3H), 1.85 (dd, $J$ = 7.2, 3.6 Hz, 3H), 1.58 (dd, $J$ = 12.4, 5.6 Hz, 3H). $^{13}$C NMR (101 MHz, $CDCl_3$) $\delta$ 158.04, 153.61, 140.73, 140.49, 139.41, 128.90, 128.21, 128.07, 126.60, 126.25, 121.42, 91.31, 55.42, 55.10, 21.97, 19.67. HRMS Calcd. for $C_{16}H_{18}N_2O_5$ $[M+H]^+$ 319.1294. Found: 319.1297.

*(R,S)-1-((Ethoxycarbonyl)oxy)ethyl 1-((R)-1-phenylethyl)-1H-imidazole-5-carboxylate (ETO-2).* Yield, 50.54%; $^{1}$H NMR (400 MHz, $CDCl_3$) $\delta$ 7.86−7.80 (m, 1H), 7.66 (d, $J$ = 1.0 Hz, 1H), 7.41−7.28 (m, 3H), 7.26−7.09 (m, 2H), 6.93 (m, 1H), 6.32 (m, 1H), 4.21 (dt, $J$ = 8.4, 7.2 Hz, 2H), 1.85 (dd, $J$ = 7.2, 3.8 Hz, 3H), 1.58 (dd, $J$ = 12.4, 5.2 Hz, 3H), 1.31 (dt, $J$ = 10.4, 7.2 Hz, 3H). $^{13}$C NMR (101 MHz, $CDCl_3$) $\delta$ 158.02, 153.03, 140.93, 140.39, 139.32, 128.83, 128.13, 128.01, 126.54, 126.22, 121.44, 91.12, 64.47, 55.44, 29.65, 22.19, 19.65, 14.09. HRMS Calcd. for $C_{17}H_{20}N_2O_5$ $[M+H]^+$ 333.1450. Found: 333.1433.

*(R,S)-1-((Isopropoxycarbonyl)oxy)ethyl 1-((R)-1-phenylethyl)-1H-imidazole-5-carboxylate (ETO-3).* Yield, 50.70%; $^{1}$H NMR (400 MHz, Chloroform-*d* ) $\delta$ 7.86−7.80 (m, 1H), 7.72 (d, $J$ = 40.0 Hz, 1H), 7.39−7.27 (m, 3H), 7.21 (dd, $J$ = 18.3, 7.4 Hz, 2H), 6.93 (q, $J$ = 5.4 Hz, 1H), 6.33 (p, $J$ = 7.2 Hz, 1H), 4.97−4.81 (m, $J$ = 6.2 Hz, 1H), 1.85 (dd, $J$ = 7.0, 3.9 Hz, 3H), 1.58 (dd, $J$ = 13.0, 5.4 Hz, 3H), 1.29 (dd, $J$ = 12.5, 6.2 Hz, 6H). $^{13}$C NMR (101 MHz, Chloroform-*d* ) $\delta$ 158.08, 157.97, 152.42, 140.86, 140.35, 139.26, 128.89, 128.20, 126.58, 126.29, 121.53, 90.80, 72.77, 55.48, 22.22, 21.61, 19.69. HRMS Calcd. for $C_{18}H_{22}N_2O_5$ $[M+H]^+$ 347.1607. Found: 347.1605.

*(R,S)-1-((sec-Butoxycarbonyl)oxy)ethyl 1-((R)-1-phenylethyl)-1H-imidazole-5-carboxylate (ETO-4).* Yield, 36.15%; $^{1}$H NMR (400 MHz, $CDCl_3$) $\delta$ 7.85−7.78 (m, 1H), 7.76 (d, $J$ = 3.7 Hz, 1H), 7.38−7.27 (m, 3H), 7.19 (d, $J$ = 7.4 Hz, 2H), 6.92 (q,

$J$ = 5.6 Hz, 1H), 6.33 (q, $J$ = 7.2 Hz, 1H), 4.73 (ddq, $J$ = 10.0, 6.4, 3.2 Hz, 1H), 1.86 (dd, $J$ = 7.2, 1.2 Hz, 3H), 1.70−1.58 (m, 2H), 1.57 (d, $J$ = 5.6 Hz, 3H), 1.28 (d, $J$ = 6.4 Hz, 3H), 0.93 (t, $J$ = 7.6 Hz, 3H). $^{13}$C NMR (101 MHz, $CDCl_3$) $\delta$ 158.02, 152.83, 152.81, 140.84, 140.43, 139.26, 128.88, 128.09, 126.33, 126.31, 121.51, 90.85, 77.42, 55.45, 28.70, 28.64, 22.22, 22.20, 19.69, 19.25, 19.22, 9.53, 9.50. HRMS Calcd. for $C_{19}H_{24}N_2O_5$ $[M+H]^+$ 361.1763. Found: 361.1752.

*(R,S)-1-((Isobutoxycarbonyl)oxy)ethyl 1-((R)-1-phenylethyl)-1H-imidazole-5-carboxylate (ETO-5).* Yield, 18.70%; $^1$H NMR (400 MHz, $CDCl_3$) $\delta$ 7.82 (d, $J$ = 0.8 Hz, 1H), 7.76 (s, 1H), 7.38−7.28 (m, 3H), 7.21−7.15 (m, 2H), 6.93 (q, $J$ = 5.4 Hz, 1H), 6.33 (q, $J$ = 7.2 Hz, 1H), 3.95 (d, $J$ = 6.8 Hz, 2H), 1.98 (dt, $J$ = 13.6, 6.8 Hz, 1H), 1.86 (d, $J$ = 7.2 Hz, 3H), 1.57 (d, $J$ = 5.6 Hz, 3H), 0.95 (d, $J$ = 6.8 Hz, 6H). $^{13}$C NMR (101 MHz, $CDCl_3$) $\delta$ 157.98, 153.28, 140.87, 140.45, 139.35, 128.88, 128.08, 126.30, 121.46, 90.97, 74.53, 55.47, 27.74, 22.23, 19.67, 18.85, 18.84. HRMS Calcd. for $C_{19}H_{24}N_2O_5$ $[M+H]^+$ 361.1763. Found: 361.1757.

*(R,S)-1-((Cyclopropoxycarbonyl)oxy)ethyl 1-((R)-1-phenylethyl)-1H-imidazole-5-carboxylate (ETO-6).* Yield, 28.71%; $^1$H NMR (400 MHz, Chloroform-*d* ) $\delta$ 7.83 (s, 1H), 7.74 (d, $J$ = 43.3 Hz, 1H), 7.34 (dq, $J$ = 13.4, 7.0 Hz, 3H), 7.21 (dd, $J$ = 19.1, 7.0 Hz, 2H), 6.93 (q, $J$ = 5.5, 4.8 Hz, 1H), 6.38−6.27 (m, 1H), 4.15 (dtd, $J$ = 12.0, 6.2, 3.2 Hz, 1H), 1.86 (dd, $J$ = 7.1, 4.6 Hz, 3H), 1.58 (dd, $J$ = 12.8, 5.4 Hz, 3H), 0.76 (tdd, $J$ = 13.1, 6.1, 3.8 Hz, 4H). $^{13}$C NMR (101 MHz, $CDCl_3$) $\delta$ 156.07, 153.34, 138.38, 138.13, 137.64, 129.46, 129.40, 129.04, 127.03, 126.79, 122.26, 92.20, 58.60, 52.68, 21.79, 19.51, 5.12. HRMS Calcd. for $C_{18}H_{20}N_2O_5$ $[M+H]^+$ 345.1450. Found: 345.1440.

*(R,S)-1-((Cyclobutoxycarbonyl)oxy)ethyl 1-((R)-1-phenylethyl)-1H-imidazole-5-carboxylate (ETO-7).* Yiled, 23.15%; $^1$H NMR (400 MHz, Chloroform-*d* ) $\delta$ 7.82 (s, 1H), 7.72 (d, $J$ = 44.2 Hz, 1H), 7.38−7.28 (m, 3H), 7.20 (dd, $J$ = 20.3, 6.9 Hz, 2H), 6.91 (q, $J$ = 5.4 Hz, 1H), 6.32 (p, $J$ = 7.1 Hz, 1H), 4.93 (h, $J$ = 7.7 Hz, 1H), 2.45−2.29 (m, 2H), 2.14 (dq, $J$ = 20.1, 10.2 Hz, 2H), 1.85 (dd, $J$ = 7.0, 4.4 Hz, 3H), 1.83−1.61 (m, 2H), 1.57 (dd, $J$ = 12.8, 5.4 Hz, 3H). $^{13}$C NMR (101 MHz, Chloroform-*d* ) $\delta$ 162.54, 158.04, 152.00, 140.88, 139.29, 128.99, 128.02, 126.59, 126.28, 90.86, 72.20, 55.42, 36.49, 29.90, 22.24, 19.69, 13.03. HRMS Calcd. for $C_{19}H_{22}N_2O_5$ $[M+H]^+$ 359.1607. Found: 359.1616.

*(R,S)-1-(((Cyclopent-3-en-1-yloxy)carbonyl)oxy)ethyl 1-((R)-1-phenylethyl)-1H-imidazole-5-carboxylate (ETO-8).* Yield, 30.78%; $^1$H NMR (400 MHz, Chloroform-*d* ) $\delta$ 7.81 (s, 1H), 7.71 (d, $J$ = 43.3 Hz, 1H), 7.39−7.28 (m, 3H), 7.21 (dd, $J$ = 20.2, 7.1 Hz, 2H), 6.91 (s, 1H), 6.32 (p, $J$ = 7.2 Hz, 1H), 5.70 (d, $J$ = 6.6 Hz, 2H), 5.31 (q, $J$ = 4.6, 2.7 Hz, 1H), 2.83−2.67 (m, 2H), 2.56−2.40 (m, 2H), 1.86 (dd, $J$ = 7.1, 4.6 Hz, 3H), 1.63−1.52 (m, 3H). $^{13}$C NMR (101 MHz, Chloroform-*d* ) $\delta$ 157.98, 152.81, 140.66, 140.45, 139.38, 128.90, 128.20, 128.05, 127.92, 126.28, 121.48, 90.89, 55.46, 39.54, 22.25, 19.68. HRMS Calcd. for $C_{20}H_{22}N_2O_5$ $[M+H]^+$ 371.1607. Found: 371.1596.

*((Methoxycarbonyl)oxy)methyl (R)-1-(1-phenylethyl)-1H-imidazole-5-carboxylate (ETO-9).* Yield, 32.80%; $^1$H NMR (400 MHz, $CDCl_3$) $\delta$ 7.88 (d, $J$ = 1.0 Hz, 1H), 7.76 (d, $J$ = 1.0 Hz, 1H), 7.38−7.28 (m, 3H), 7.23−7.16 (m, 2H), 6.30 (q, $J$ = 7.2 Hz, 1H), 5.94 (d, $J$ = 5.8 Hz, 1H), 5.85 (d, $J$ = 5.8 Hz, 1H), 3.84 (s, 3H), 1.86 (d, $J$ = 7.2 Hz, 3H). $^{13}$C NMR (101 MHz, $CDCl_3$) $\delta$ 158.31, 154.51, 140.80, 140.65, 139.90, 128.91, 128.16, 126.33, 121.13, 81.61, 55.62, 55.34, 22.18. HRMS Calcd. for $C_{15}H_{16}N_2O_5$ $[M+H]^+$ 305.1137. Found: 305.1138.

*((Ethoxycarbonyl)oxy)methyl (R)-1-(1-phenylethyl)-1H-imidazole-5-carboxylate (ETO-10).* Yield, 33.70%; $^1$H NMR (400 MHz, $CDCl_3$) $\delta$ 7.88 (d, $J$ = 1.0 Hz, 1H), 7.76 (d, $J$ = 1.0 Hz, 1H), 7.38−7.28 (m, 3H), 7.23−7.16 (m, 2H), 6.30 (q, $J$ = 7.2 Hz, 1H), 5.94 (d, $J$ = 5.8 Hz, 1H), 5.85 (d, $J$ = 5.8 Hz, 1H), 3.84 (s, 3H), 1.86 (d, $J$ = 7.2 Hz, 3H). $^{13}$C NMR (101 MHz, $CDCl_3$) $\delta$ 156.24, 153.49, 138.54, 137.84, 129.40, 129.31, 128.08, 126.85, 122.09, 82.20, 65.31, 59.21, 22.05, 14.07. HRMS Calcd. for $C_{16}H_{18}N_2O_5$ $[M+H]^+$ 319.1294. Found: 319.1293.

*((tert-Butoxycarbonyl)oxy)methyl (R)-1-(1-phenylethyl)-1H-imidazole-5-carboxylate (ETO-11).* Yield, 35.30%; $^1$H NMR (400 MHz, $CDCl_3$) $\delta$ 7.87 (s, 1H), 7.75 (s, 1H), 7.41−7.27 (m, 3H), 7.24−7.12 (m, 2H), 6.32 (q, $J$ = 7.2 Hz, 1H), 5.88 (d, $J$ = 5.8 Hz, 1H), 5.81 (d, $J$ = 5.8 Hz, 1H), 1.86 (d, $J$ = 7.2 Hz, 3H), 1.50 (s, 9H). $^{13}$C NMR (101 MHz, $CDCl_3$) $\delta$ 158.49, 151.95, 140.67, 139.72, 128.90, 128.15, 126.36, 121.32, 83.68, 81.08, 55.55, 27.62, 22.18. HRMS Calcd. for $C_{18}H_{22}N_2O_5$ $[M+H]^+$ 347.1607. Found: 347.1610.

*((Isobutoxycarbonyl)oxy)methyl (R)-1-(1-phenylethyl)-1H-imidazole-5-carboxylate (ETO-12).* Yield, 81.70%; $^1$H NMR (400 MHz, $CDCl_3$) $\delta$ 7.88 (d, $J$ = 0.8 Hz, 1H), 7.77 (s, 1H), 7.25−7.33 (m, 3H), 7.22−7.17 (m, 2H), 6.31 (q, $J$ = 7.2 Hz, 1H), 5.94 (d, $J$ = 5.8 Hz, 1H), 5.85 (d, $J$ = 5.8 Hz, 1H), 3.98 (d, $J$ = 6.8 Hz, 2H), 1.99 (dp, $J$ = 13.6, 6.8 Hz, 1H), 1.86 (d, $J$ = 7.2 Hz, 3H), 0.95 (d, $J$ = 6.8 Hz, 6H). $^{13}$C NMR (101 MHz, $CDCl_3$) $\delta$ 158.38, 154.03, 140.77, 140.66, 139.89, 128.91, 128.15, 126.34, 121.19, 81.54, 74.79, 55.60, 27.71, 22.19, 18.82. HRMS Calcd. for $C_{18}H_{22}N_2O_5$ $[M+H]^+$ 347.1607. Found: 347.1602.

*(R,S)-((sec-Butoxycarbonyl)oxy)methyl 1-((R)-1-phenylethyl)-1H-imidazole-5-carboxylate (ETO-13).* Yield, 35.32%; $^1$H NMR (400 MHz, $CDCl_3$) $\delta$ 9.82 (s, 1H), 8.08 (s, 1H), 7.50−7.30 (m, 5H), 6.47 (q, $J$ = 6.8 Hz, 1H), 5.97 (d, $J$ = 5.8 Hz, 1H), 5.90 (dd, $J$ = 5.8, 1.0 Hz, 1H), 4.77 (h, $J$ = 6.2 Hz, 1H), 2.09 (d, $J$ = 7.2 Hz, 3H), 1.75−1.53 (m, 2H), 1.30 (dd, $J$ = 6.4, 1.2 Hz, 3H), 0.93 (td, $J$ = 7.6, 2.2 Hz, 3H). $^{13}$C NMR (101 MHz, $CDCl_3$) $\delta$ 156.28, 153.19, 138.40, 137.70, 129.47, 129.42, 127.95, 126.90, 122.15, 82.19, 78.47, 59.20, 28.58, 22.02, 19.17, 9.47. HRMS Calcd. for $C_{18}H_{22}N_2O_5$ $[M+H]^+$ 347.1607. Found: 347.1591.

*((Cyclobutoxycarbonyl)oxy)methyl (R)-1-(1-phenylethyl)-1H-imidazole-5-carboxylate (ETO-14).* Yield, 30.12%; $^1$H NMR (400 MHz, $CDCl_3$) $\delta$ 7.87 (d, $J$ = 1.0 Hz, 1H), 7.76 (d, $J$ = 1.0 Hz, 1H), 7.33 (m, 3H), 7.23−7.18 (m, 2H), 6.30 (q, $J$ = 7.2 Hz, 1H), 5.91 (d, $J$ = 5.8 Hz, 1H), 5.84 (d, $J$ = 5.8 Hz, 1H), 5.01−4.92 (m, 1H), 2.42−2.32 (m, 2H), 2.21−2.07 (m, 2H), 1.86 (d, $J$ = 7.2 Hz, 3H), 1.81 (dtt, $J$ = 10.0, 2.8, 1.2 Hz, 1H), 1.66−1.56 (m, 1H). $^{13}$C NMR (101 MHz, $CDCl_3$) $\delta$ 156.57, 152.62, 139.05, 138.03, 129.96, 129.47, 129.32, 126.90, 122.11, 82.14, 72.88, 58.70, 29.92, 22.24, 12.98. HRMS Calcd. for $C_{18}H_{20}N_2O_5$ $[M+H]^+$ 345.1450. Found: 345.1443.

*(((Cyclopent-3-en-1-yloxy)carbonyl)oxy)methyl (R)-1-(1-phenylethyl)-1H-imidazole-5-carboxylate (ETO-15).* Yield, 32.18%; $^1$H NMR (400 MHz, $CDCl_3$) $\delta$ 7.87 (d, $J$ = 1.0 Hz, 1H), 7.76 (d, $J$ = 1.0 Hz, 1H), 7.40−7.27 (m, 3H), 7.23−7.13 (m, 2H), 6.30 (q, $J$ = 7.2 Hz, 1H), 5.92 (d, $J$ = 5.8 Hz, 1H), 5.84 (d, $J$ = 5.8 Hz, 1H), 5.70 (s, 2H), 5.33 (tt, $J$ = 6.8, 2.4 Hz, 1H), 2.84−2.69 (m, 2H), 2.57−2.44 (m, 2H), 1.86 (d, $J$ = 7.2 Hz, 3H). $^{13}$C NMR (101 MHz, $CDCl_3$) $\delta$ 158.35, 153.68, 140.77, 140.65, 139.85, 128.92, 128.16, 127.97, 126.35, 121.20, 81.46, 79.08, 55.60, 39.50, 39.49, 22.19. HRMS Calcd. for $C_{19}H_{20}N_2O_5$ $[M+H]^+$ 357.1450. Found: 357.1451.

*(R,S)-(((But-3-en-2-yloxy)carbonyl)oxy)methyl 1-((R)-1-phenylethyl)-1H-imidazole-5-carboxylate (ETO-16).* Yield,

30.01%; $^1$H NMR (400 MHz, Chloroform-*d* ) $\delta$ 7.87 (s, 1H), 7.76 (s, 1H), 7.32 (dd, $J$ = 14.0, 7.2 Hz, 3H), 7.20 (d, $J$ = 7.3 Hz, 2H), 6.31 (q, $J$ = 7.1 Hz, 1H), 5.93 (t, $J$ = 6.0 Hz, 1H), 5.85 (td, $J$ = 11.8, 11.0, 5.3 Hz, 2H), 5.35−5.17 (m, 3H), 1.86 (d, $J$ = 7.1 Hz, 3H), 1.39 (d, $J$ = 6.5 Hz, 3H). $^{13}$C NMR (101 MHz, $CDCl_3$) $\delta$ 158.37, 153.18, 140.77, 140.66, 139.89, 136.46, 128.91, 128.16, 126.35, 121.20, 117.14, 117.11, 81.50, 76.29, 55.59, 22.18, 19.89. HRMS Calcd. for $C_{18}H_{20}N_2O_5$ $[M+H]^+$ 345.1450. Found: 345.1440.

*(R,S)-(((1-Phenylethoxy)carbonyl)oxy)methyl 1-((R)-1-phenylethyl)-1H-imidazole-5-carboxylate (ETO-17).* Yield, 36.10%; $^1$H NMR (400 MHz, $CDCl_3$) $\delta$ 7.84 (dd, $J$ = 1.6, 0.8 Hz, 1H), 7.75 (s, 1H), 7.40−7.27 (m, 8H), 7.22−7.13 (m, 2H), 6.29 (q, $J$ = 7.0 Hz, 1H), 5.91 (dd, $J$ = 14.8, 5.8 Hz, 1H), 5.79 (ddd, $J$ = 24.8, 13.2, 6.2 Hz, 2H), 1.85 (dd, $J$ = 7.2, 1.2 Hz, 3H), 1.61 (d, $J$ = 6.6 Hz, 3H). $^{13}$C NMR (101 MHz, $CDCl_3$) $\delta$ 158.35, 153.25, 140.77, 140.67, 140.38, 139.91, 128.92, 128.64, 128.41, 128.17, 126.37, 126.35, 126.10, 126.09, 121.18, 81.55, 77.55, 55.60, 22.20. HRMS Calcd. for $C_{22}H_{22}N_2O_5$ $[M+H]^+$ 395.1607. Found: 395.1601.

*((((3-Methylbut-2-en*-1-yl*)oxy)carbonyl)oxy)methyl(R)-1-(1-phenylethyl)-1H-imidazole-5-carboxylate (ETO-18).* Yield, 25.78%; $^1$H NMR (400 MHz, $CDCl_3$) $\delta$ 7.87 (d, $J$ = 0.8 Hz, 1H), 7.76 (s, 1H), 7.38−7.28 (m, 3H), 7.23−7.16 (m, 2H), 6.30 (q, $J$ = 7.2 Hz, 1H), 5.93 (d, $J$ = 5.8 Hz, 1H), 5.85 (d, $J$ = 5.8 Hz, 1H), 5.37 (tt, $J$ = 7.2, 1.2 Hz, 1H), 4.68 (d, $J$ = 7.4 Hz, 2H), 1.86 (d, $J$ = 7.2 Hz, 3H), 1.74 (d, $J$ = 15.2 Hz, 6H). $^{13}$C NMR (101 MHz, $CDCl_3$) $\delta$ 158.36, 153.97, 140.86, 140.76, 139.88, 128.92, 128.16, 126.36, 121.21, 117.42, 81.54, 65.42, 55.58, 25.78, 22.18, 18.10. HRMS Calcd. for $C_{19}H_{22}N_2O_5$ $[M+H]^+$ 359.1607. Found: 359.1596.

*(((Octadecyloxy)carbonyl)oxy)methyl (R)-1-(1-phenylethyl)-1H-imidazole-5-carboxylate (ETO-19).* Yield, 45.50%; $^1$H NMR (400 MHz, $CDCl_3$) $\delta$ 7.88 (d, $J$ = 0.8 Hz, 1H), 7.79−7.69 (m, 1H), 7.33 (m, 3H), 7.23−7.17 (m, 2H), 6.31 (q, $J$ = 7.2 Hz, 1H), 5.93 (d, $J$ = 5.8 Hz, 1H), 5.85 (d, $J$ = 5.8 Hz, 1H), 4.18 (t, $J$ = 6.8 Hz, 2H), 1.86 (d, $J$ = 7.2 Hz, 3H), 1.70−1.63 (m, 2H), 1.25 (m, 30H), 0.90−0.85 (m, 3H). $^{13}$C NMR (101 MHz, $CDCl_3$) $\delta$ 158.37, 153.99, 140.75, 139.86, 128.91, 128.16, 126.35, 121.19, 81.51, 69.03, 55.60, 31.94, 29.71, 29.67, 29.64, 29.56, 29.48, 29.37, 29.19, 28.50, 25.62, 22.70, 22.19, 14.14. HRMS Calcd. for $C_{32}H_{50}N_2O_5$ $[M+H]^+$ 543.3798. Found: 543.3793.

*(R,S)-1-((Methoxycarbonyl)oxy)propyl 1-((R)-1-phenylethyl)-1H-imidazole-5-carboxylate (ETO-20).* Yield, 19.40%;$^1$H NMR (400 MHz, Chloroform-*d* ) $\delta$ 7.83 (d, $J$ = 2.6 Hz, 1H), 7.71 (d, $J$ = 46.1 Hz, 1H), 7.33 (dq, $J$ = 13.7, 7.2 Hz, 3H), 7.21 (dd, $J$ = 20.1, 7.2 Hz, 2H), 6.80 (q, $J$ = 5.3 Hz, 1H), 6.33 (p, $J$ = 7.2 Hz, 1H), 3.80 (d, $J$ = 10.9 Hz, 3H), 1.91 (dd, $J$ = 13.9, 6.8 Hz, 2H), 1.86 (dd, $J$ = 7.1, 3.2 Hz, 3H), 0.99 (dt, $J$ = 15.4, 7.5 Hz, 3H). $^{13}$C NMR (101 MHz, Chloroform-*d* ) $\delta$ 158.11, 153.98, 140.84, 140.47, 139.26, 128.91, 128.09, 126.64, 121.47, 93.96, 55.49, 55.12, 26.63, 22.21, 7.56. HRMS Calcd. for $C_{17}H_{20}N_2O_5$ $[M+H]^+$ 333.1450. Found: 333.1451.

*(R,S)-1-((Ethoxycarbonyl)oxy)propyl 1-((R)-1-phenylethyl)-1H-imidazole-5-carboxylate (ETO-21).* Yield, 14.90%; $^1$H NMR (400 MHz, Chloroform-*d* ) $\delta$ 7.82 (d, $J$ = 3.7 Hz, 1H), 7.70 (d, $J$ = 42.3 Hz, 1H), 7.37−7.27 (m, 3H), 7.20 (dd, $J$ = 19.2, 7.0 Hz, 2H), 6.80 (q, $J$ = 5.3 Hz, 1H), 6.32 (p, $J$ = 7.1 Hz, 1H), 4.29−4.13 (m, 2H), 1.92 (dt, $J$ = 14.9, 7.5 Hz, 2H), 1.85 (dd, $J$ = 7.0, 3.1 Hz, 3H), 1.30 (dt, $J$ = 14.1, 7.1 Hz, 3H), 1.05−0.93 (m, 3H). $^{13}$C NMR (101 MHz, Chloroform-*d* ) $\delta$ 158.27, 153.33, 140.88, 140.34, 139.29, 128.89, 128.20, 126.31, 121.50, 93.79, 64.53, 55.37, 26.66, 22.20, 14.11, 7.58. HRMS Calcd. for $C_{18}H_{22}N_2O_5$ $[M+H]^+$ 347.1607. Found: 347.1604.

*(R,S)-1-((Isopropoxycarbonyl)oxy)propyl 1-((R)-1-phenylethyl)-1H-imidazole-5-carboxylate (ETO-22).* Yield, 19.70%; $^1$H NMR (400 MHz, Chloroform-*d* ) $\delta$ 7.81 (d, $J$ = 5.2 Hz, 1H), 7.71 (d, $J$ = 35.6 Hz, 1H), 7.32 (dq, $J$ = 13.7, 6.8 Hz, 3H), 7.21 (dd, $J$ = 17.1, 7.9 Hz, 2H), 6.79 (q, $J$ = 5.4 Hz, 1H), 6.33 (p, $J$ = 7.1 Hz, 1H), 4.95−4.81 (m, 1H), 1.91 (dt, $J$ = 15.1, 7.6 Hz, 2H), 1.85 (dd, $J$ = 7.1, 3.5 Hz, 3H), 1.36−1.21 (m, 6H), 0.98 (dt, $J$ = 18.0, 7.5 Hz, 3H). $^{13}$C NMR (101 MHz, Chloroform-*d* ) $\delta$158.18, 152.68, 140.85, 140.37, 139.15, 128.89, 128.19, 126.34, 121.56, 93.70, 72.74, 55.38, 26.68, 22.16, 21.60, 7.60. HRMS Calcd. for $C_{19}H_{24}N_2O_5$ $[M+H]^+$ 361.1763. Found: 361.1763.

*(R,S)-1-((tert-Butoxycarbonyl)oxy)propyl 1-((R)-1-phenylethyl)-1H-imidazole-5-carboxylate (ETO-23).* Yield, 15.10%; $^1$H NMR (400 MHz, $CDCl_3$) $\delta$ 7.81 (d, $J$ = 7.6 Hz, 1H), 7.76 (s, 1H), 7.68 (s, 1H), 7.32 (m, 3H), 7.25−7.15 (m, 2H), 6.76 (td, $J$ = 5.6, 2.4 Hz, 1H), 6.34 (p, $J$ = 7.2 Hz, 1H), 1.88 (m, 5H), 1.47 (d, $J$ = 16.4 Hz, 9H), 0.98 (dt, $J$ = 22.0, 7.6 Hz, 3H). $^{13}$C NMR (101 MHz, $CDCl_3$) $\delta$ 158.35, 151.38, 140.90, 140.51, 139.17, 128.86, 128.13, 128.05, 126.54, 126.33, 121.64, 93.48, 83.24, 55.35, 27.60, 26.68, 22.02, 7.75. HRMS Calcd. for $C_{20}H_{26}N_2O_5$ $[M+H]^+$ 375.1920. Found: 375.1919.

#### *4.2.2. General procedure for preparation of compounds ETO-24−ETO-27 (with ETO-24 as an example)*

As shown in Scheme 2, to a 100 mL round-bottomed flask, ET-COOH (797.49 mg, 3.69 mmol) was dissolved in DMF (10 mL), then $K_2CO_3$ (1.5 g, 10.85 mmol) was added into the reaction stirred for 10 min. Commercially available compound **4a** (500 mg, 4.61 mmol) was dissolved in DMF (1 mL) and dropped to the reaction stirred overnight. After that, 100 mL water was poured into the reaction and 80 mL ethyl acetate was used to extracted twice, combined the organic phases and wash twice with water, retained organic phase and distilled off under reduced pressure to obtain crude target compound. The crude product was purified by column chromatography to obtain compound ETO-24.

*Acetoxymethyl (R)-1-(1-phenylethyl)-1H-imidazole-5-carboxylate (ETO-24).* Yield, 55.10%; $^1$H NMR (400 MHz, Chloroform-*d* ) $\delta$ 7.87 (s, 1H), 7.77 (d, $J$ = 1.0 Hz, 1H), 7.38−7.28 (m, 3H), 7.22−7.17 (m, 2H), 6.30 (q, $J$ = 7.1 Hz, 1H), 5.93−5.82 (m, 2H), 2.11 (s, 3H), 1.87 (d, $J$ = 7.1 Hz, 3H). 13C NMR (101 MHz, Chloroform-*d* ) $\delta$ 169.59, 158.65, 140.75, 140.70, 139.79, 128.91, 128.14, 126.31, 121.31, 78.84, 55.66, 22.24, 20.76. HRMS Calcd. for $C_{15}H_{16}N_2O_4$ $[M+H]^+$ 289.1188. Found: 289.1197.

*2-Acetoxyethyl (R)-1-(1-phenylethyl)-1H-imidazole-5-carboxylate (ETO-25).* Yield, 58.30%; $^1$H NMR (400 MHz, Chloroform-*d* ) $\delta$ 7.80 (s, 1H), 7.74 (d, $J$ = 1.0 Hz, 1H), 7.38−7.28 (m, 3H), 7.20−7.15 (m, 2H), 6.33 (q, $J$ = 7.1 Hz, 1H), 4.41 (tt, $J$ = 4.0, 2.1 Hz, 2H), 4.36−4.30 (m, 2H), 2.05 (s, 3H), 1.87 (d, $J$ = 7.1 Hz, 3H). $^{13}$C NMR (101 MHz, Chloroform-*d* ) $\delta$170.81, 159.87, 141.02, 140.08, 138.67, 128.89, 128.05, 126.23, 122.06, 62.05, 55.47, 22.24, 20.80. HRMS Calcd. for $C_{16}H_{18}N_2O_4$ $[M+H]^+$ 303.1345. Found: 303.1339.

*3-Acetoxypropyl (R)-1-(1-phenylethyl)-1H-imidazole-5-carboxylate (ETO-26).*Yield, 65.30%; $^1$H NMR (400 MHz, Chloroform-*d* ) $\delta$ 7.77 (s, 1H), 7.73 (s, 1H), 7.37−7.28 (m, 3H), 7.18 (d, $J$ = 7.1 Hz, 2H), 6.34 (q, $J$ = 7.1 Hz, 1H), 4.36−4.23 (m, 2H), 4.16 (t, $J$ = 6.3 Hz, 2H), 2.04 (d, $J$ = 3.6 Hz, 5H), 1.86 (d, $J$ = 7.1 Hz, 3H). $^{13}$C NMR (101 MHz, Chloroform-*d* ) $\delta$ 170.99,

160.08, 141.01, 139.96, 138.15, 128.88, 128.05, 126.25, 122.33, 61.14, 61.06, 55.45, 28.00, 22.23, 20.90. HRMS Calcd. for $C_{17}H_{21}N_2O_4$ $[M+H]^+$ 317.1501. Found: 317.1480.

*1-Acetoxyethyl 1-((R)-1-phenylethyl)-1H-imidazole-5-carboxylate (ETO-27).* Yield, 61.10%; $^1$H NMR (400 MHz, Chloroform-*d* ) $\delta$ 7.81 (s, 1H), 7.72 (d, $J$ = 32.0 Hz, 1H), 7.37−7.28 (m, 3H), 7.24−7.16 (m, 2H), 7.03 (t, $J$ = 5.5 Hz, 1H), 6.37−6.27 (m, 1H), 2.06 (d, $J$ = 22.0 Hz, 3H), 1.86 (dd, $J$ = 7.1, 3.6 Hz, 3H), 1.54 (dd, $J$ = 11.2, 5.5 Hz, 3H). $^{13}$C NMR (101 MHz, Chloroform-*d* ) $\delta$ 168.99, 157.96, 140.78, 140.42, 138.91, 128.89, 128.21, 126.55, 126.31, 88.37, 55.55, 22.22, 20.90, 19.61. HRMS Calcd. for $C_{19}H_{22}N_2O_5$ $[M+H]^+$ 303.1345. Found: 303.1334.

#### 4.2.3. General procedure for preparation of compounds ETO-28−ETO-32 (with ETO-28 as an example)

In Scheme 3, ET-COOH (797.49 mg, 3.69 mmol) was dissolved in DMF (10 mL) to a 100 mL round-bottomed flask, then $K_2CO_3$ (1.5 g, 10.85 mmol) was added into the reaction stirred for 10 min. Commercially available compound **5a** (480 mg, 4.4 mmol) was dissolved in DMF (1 mL) and dropped to the reaction stirred overnight. After that, 100 mL water was poured into the reaction and 80 mL ethyl acetate was used to extracted twice, combined the organic phases and wash twice with water, retained organic phase and distilled off under reduced pressure to obtain crude target compound. The crude product was purified by column chromatography to obtain compound ETO-28.

*3-Methoxypropyl (R)-1-(1-phenylethyl)-1H-imidazole-5-carboxylate (ETO-28).* Yield, 65.40%; $^1$H NMR (400 MHz, Chloroform-*d* ) $\delta$ 7.76 (s, 1H), 7.72 (d, $J$ = 1.1 Hz, 1H), 7.32 (dt, $J$ = 14.7, 7.2 Hz, 3H), 7.18 (d, $J$ = 7.7 Hz, 2H), 6.36 (q, $J$ = 7.1 Hz, 1H), 4.31 (tt, $J$ = 10.7, 5.5 Hz, 2H), 3.46 (t, $J$ = 6.2 Hz, 2H), 3.32 (s, 3H), 1.95 (p, $J$ = 6.3 Hz, 2H), 1.86 (d, $J$ = 7.1 Hz, 3H). $^{13}$C NMR (101 MHz, Chloroform-*d* ) $\delta$160.24, 141.12, 139.82, 138.12, 128.85, 128.00, 126.28, 122.52, 69.04, 61.60, 58.73, 55.33, 29.00, 22.22. HRMS Calcd. for $C_{16}H_{20}N_2O_3$ $[M+H]^+$ 289.1552. Found: 289.1568.

*2-(2-Methoxyethoxy)ethyl (R)-1-(1-phenylethyl)-1H-imidazole-5-carboxylate (ETO-29).* Yield, 60.20%; $^1$H NMR (400 MHz, Chloroform-*d* ) $\delta$ 7.81 (d, $J$ = 1.0 Hz, 1H), 7.72 (s, 1H), 7.37−7.28 (m, 3H), 7.21−7.15 (m, 2H), 6.34 (q, $J$ = 7.1 Hz, 1H), 4.42−4.32 (m, 2H), 3.76 (t, $J$ = 4.8 Hz, 2H), 3.65 (dd, $J$ = 5.7, 3.6 Hz, 2H), 3.54 (dd, $J$ = 5.6, 3.6 Hz, 2H), 3.37 (s, 3H), 1.86 (d, $J$ = 7.1 Hz, 3H). $^{13}$C NMR (101 MHz, Chloroform-*d* ) $\delta$ 160.13, 141.10, 139.91, 138.54, 128.85, 128.00, 126.28, 122.36, 71.92, 70.62, 69.11, 63.57, 59.09, 55.39, 22.22. HRMS Calcd. for $C_{17}H_{22}N_2O_4$ $[M+H]^+$ 319.1658. Found: 319.1634.

*2-(2-Ethoxyethoxy)ethyl (R)-1-(1-phenylethyl)-1H-imidazole-5-carboxylate (ETO-30).* Yield, 63.10%; $^1$H NMR (400 MHz, Chloroform-*d* ) $\delta$ 7.83−7.78 (m, 1H), 7.72 (d, $J$ = 1.0 Hz, 1H), 7.37−7.27 (m, 3H), 7.21−7.16 (m, 2H), 6.34 (q, $J$ = 7.1 Hz, 1H), 4.37 (q, $J$ = 4.7 Hz, 2H), 3.76 (t, $J$ = 4.9 Hz, 2H), 3.66 (dd, $J$ = 6.0, 3.5 Hz, 2H), 3.58 (dd, $J$ = 6.0, 3.5 Hz, 2H), 3.52 (q, $J$ = 7.0 Hz, 2H), 1.86 (d, $J$ = 7.1 Hz, 3H), 1.20 (t, $J$ = 7.0 Hz, 3H). $^{13}$C NMR (101 MHz, Chloroform-*d* ) $\delta$ 160.15, 141.11, 139.90, 138.55, 128.85, 128.00, 126.28, 122.37, 70.78, 69.85, 69.09, 66.72, 63.60, 55.39, 22.23, 15.16. HRMS Calcd. for $C_{18}H_{24}N_2O_4$ $[M+H]^+$ 333.1814. Found: 333.1823.

*(R)-4-Ethoxy-1-(1-(1-phenylethyl)-1H-imidazole-5-yl)butan-1-one (ETO-31).* Yield, 67.44%; $^1$H NMR (400 MHz, Chloroform-*d* ) $\delta$ 7.76 (s, 1H), 7.72 (s, 1H), 7.38−7.27 (m, 3H), 7.18 (d, $J$ = 7.1 Hz, 2H), 6.36 (q, $J$ = 7.1 Hz, 1H), 4.37−4.24 (m, 2H), 3.53−3.49 (m, 2H), 3.49−3.43 (m, 2H), 1.96 (p, $J$ = 6.3 Hz, 2H), 1.86 (d, $J$ = 7.1 Hz, 3H), 1.18 (t, $J$ = 7.0 Hz, 3H). $^{13}$C NMR (101 MHz, Methanol-$d_4$) $\delta$157.88, 139.35, 137.55, 128.83, 128.46, 127.57, 126.15, 124.19, 66.40, 65.89, 63.17, 58.59, 28.48, 20.80, 14.04. HRMS Calcd. for $C_{17}H_{22}N_2O_3$ $[M+H]^+$ 303.1708. Found: 303.1686.

*(R)-3-Ethoxy-1-(1-(1-phenylethyl)-1H-imidazole-5-yl)propan-1-one (ETO-32).* Yield, 63.50%; $^1$H NMR (400 MHz, Chloroform-*d* ) $\delta$ 7.82 (s, 1H), 7.72 (s, 1H), 7.36−7.27 (m, 3H), 7.20 (s, 2H), 6.35 (q, $J$ = 7.1 Hz, 1H), 4.35 (q, $J$ = 4.9 Hz, 2H), 3.68 (t, $J$ = 4.9 Hz, 2H), 3.54 (q, $J$ = 7.0 Hz, 2H), 1.86 (d, $J$ = 7.1 Hz, 3H), 1.20 (t, $J$ = 7.0 Hz, 3H). $^{13}$C NMR (101 MHz, Methanol-$d_4$) $\delta$ 157.45, 139.10, 137.45, 128.85, 128.54, 127.21, 126.23, 124.17, 67.62, 66.15, 64.78, 58.79, 20.74, 13.99. HRMS Calcd. for $C_{16}H_{20}N_2O_3$ $[M+H]^+$ 289.1552. Found: 289.1568.

### 4.3. Molecular docking and molecular dynamics simulation

The crystal structure of the human $GABA_A$ receptor alpha1-beta2-gamma2 subtype in complex with etomidate (PDB ID: 6x3v)[14] and human CYP11B1 crystal structure (PDB 6M7X)[60] were obtained from the Protein Data Bank and served as the reference structure[14]. For $GABA_A$ receptor the binding site was found to exist between specific subunits (alpha1 and beta2) within $GABA_A$ receptor. The structures of the designed etomidate derivatives were optimized. The docking comparison between ETO-4 and ET explains the loss of CYP11B1 inhibitory activity. The low-energy conformations of all molecules were generated using the "Prepare Ligands" module. Following this, the ligands were docked into the binding sites utilizing the CDOCKER docking program with the "CDOCKER ENERGY" function in Discovery Studio 2020 (Accelrys, San Diego, CA, USA), which is commonly employed for the fine docking process in lead optimization.

To further assess the activity advantages of the etomidate derivatives, we systematically evaluated the affinities of ET, ETO-1 and the candidate compound ETO-4 with $GABA_A$ receptor through molecular dynamics simulations and binding free energy calculations. The protein−ligand complex systems were conveniently constructed using CHARMM-GUI[61]. The initial structures of the protein−ligand complexes were obtained from docking, and the complexes were subsequently constructed and optimized using the CHARMM36 and CGenFF force fields, respectively[62,63]. These complexes were embedded in a 1-palmitoyl-2-oleoyl phosphatidylcholine (POPC) bilayer. The system was solvated using the TIP3 water model and neutralized with potassium and chloride ions. Prior to production simulations, a minimization step was performed to eliminate unnatural collisions, utilizing the steepest descent algorithm. Following this, a 250 ps equilibration process was conducted, gradually releasing the scaling restraint until it was fully removed. The MD simulation was carried out under NPT conditions at a temperature of 303.15 K and a pressure of 1 atm, employing a time step of 2 fs and constraining bonds involving hydrogen atoms using the LINCS algorithm. The particle mesh Ewald (PME) method was implemented to calculate electrostatic interactions. Finally, a 200 ns MD simulation was executed, and the RMSD per residue was calculated based on all atoms after trajectory alignment. To estimate the interaction free energies, we employed Molecular Mechanics Poisson-Boltzmann Surface Area (MM-PBSA) and Molecular Mechanics with Generalized Born Surface Area (MM-GBSA) methods. The calculations were performed locally, with the binding free energy of the complex determined using the "gmx_mmpbsa" tool by

analyzing 100 frames extracted from the last 10 ns of the equilibrium stage MD trajectory[64]. All simulations were conducted using the Gromacs software package, version 2021.6[65]. Additionally, all figures were created in ChimeraX, with annotations added for key interactions.

### 4.4. Stability and solubility assay

#### 4.4.1. Stability assay

All the compounds were dissolved in PBS. Let it stand at room temperature for 4 h, and measure the compound content through HPLC (Agilent 1100 series; Agilent Technologies, Santa Clara, CA, USA).

$$\text{Remaining compound ratio}\,(\%) = \frac{4-\text{Hour compound peak area}/4-\text{Hour total area}}{0-\text{Hour compound peak area}/0\,\text{Hour total area}} \times 100 \quad (2)$$

The liquid chromatography conditions were as follows: column: Swell ChromPlus C18 column (4.66 mm × 150 mm, 5 μm); Column temperature: 30 °C; Detection wavelength: 254 nm; Flow rate: 1.0 mL/min; Sample volume: 5 μL; Mobile phase: $H_2O$ (solvent A)-acetonitrile (solvent B). The gradient elution program was set as follows: 0−5.0 min 90% → 80% A; 5.0−10.0 min 80%→ 40% A; 10.0−12.0 min 40% A→10% A; 12.0−14.0 min 10%→ 90% A; 14.0−15.0 min 90% A. All compounds are operated in parallel 2 times.

#### 4.4.2. Solubility assay

Weigh 1 mg of the compound and dissolve it in 200 μL of methanol as the standard working solution. Dissolve the excess compound separately in a mixed solution of 20 μL PEG400 and 180 μL PBS to prepare a supersaturated solution. Measure the compound content in different solutions using HPLC (Agilent 1100 series; Agilent Technologies, Santa Clara, CA, USA).

$$\text{Concentration} = \frac{\text{Peak area of supersaturated solution}}{\text{Peak area of methanol solution}} \times \text{Compound concentration of methanol solution} \quad (3)$$

The liquid chromatography conditions were the same as before.

### 4.5. Animals

All experimental protocols were approved by the Institutional Animal Care and Use Committee of Sichuan University West China Hospital (20220706003, China). Animal experiments were conducted in strict accordance with the National Institutes of Health Guide for the Care and Use of Laboratory Animals. ICR mice (25 ± 2 g) and Sprague Dawley rats (250 ± 10 g) were purchased from Chengdu Dossy Biological Technology Co. Ltd. (Chengdu, China). The animals had unrestricted access to clean water and food and were housed in a conventional facility at 22 ± 2 °C on a 12-h light/dark cycle.

### 4.6. Metabolism assay

#### 4.6.1. Plasma decomposition assay

The preparation of the sample and the measurement of drug by HPLC were based on the previously described methods[66,67].

*4.6.1.1. Sample handling.* The rat plasma was obtained from 9 rats under deep anesthesia induced by isoflurane. 0.02 mmol of each compound was accurately weighed, and 50 μL acetonitrile was added to dissolve, then, added another 450 μL water to prepare a sample solution of 0.04 mmol/mL 900 μL rat plasma warmed at 37 °C for 15 min. And 100 μL sample solution of each compound was added to the plasma to obtain a final concentration of 0.004 mmol/mL. At 0, 5, 10, 20, 40, and 60 min, 100 μL plasma solution was taken and stopped with 300 μL acetonitrile for each sample to stop the drug metabolism. Samples were temporarily stored at 4 °C.

*4.6.1.2. Measurement of drug by HPLC.* When all the samples were collected, centrifugation was performed at 36,670×*g* at 4 °C for 15 min. 100 μL supernatant of each sample was analyzed by HPLC (Agilent 1100 series; Agilent Technologies, Santa Clara, CA, USA). The liquid chromatography conditions were as follows: column: Swell ChromPlus C18 column (4.66 mm × 150 mm, 5 μm); Column temperature: 30 °C; Detection wavelength: 254 nm; Flow rate: 1.0 mL/min; Sample volume: 5 μL; Mobile phase: acetonitrile (solvent A) 0.1% trifluoroacetic acid aqueous (solvent B). The gradient elution program was set as follows: 0−5.0 min 10% → 90% A; 5.0−10.0 min 90% A; 10.0−13.0 min 90% A→10% A; 13.0−15.0 min 10% A. All compounds are operated in parallel 3 times. The metabolic rate of each compound was calculated by the peak area.

$$\text{Metabolic rate}(\%) = \text{metabolite peak area}/\text{total peak area} \times 100 \quad (4)$$

#### 4.6.2. In vivo metabolism assay

Preparation of standard curve working solution: 2.5/5/25/50/250/500/2000/2500 ng/mL, quality control working solution: 7.5/125/1875 ng/mL (diluent: 50% acetonitrile).

Preparation of standard curve: 0.5/1/5/10/50/100/400/500 ng/mL, quality control: 1.5/25/375 ng/mL (diluent: ICR mouse whole blood).

Blood collection: ICR mice were used, and 20 μL of whole blood was taken from the hind limb saphenous vein immediately after administration at 0, 1, 2, 3, 4, 5, 7, and 10 min. Protein precipitation was immediately performed after collection.

Centrifuge: Add 100 μL of internal standard working solution (Double BLK replaced with 80% acetonitrile/20% methanol) to 10 μL of biological samples (Double BLK and BLK replaced with blank biological matrix). After mixing, centrifuge at 4 °C 1467×*g* for 10 min, take 50 μL of the supernatant and add 100 μL of 0.1% formic acid water, mix well.

Use liquid chromatography−mass spectrometry (LC−MS) for sample injection detection.

Liquid phase analysis conditions (LC-30AD, SCIEX): column: Titank C18 3u (2.1 mm × 50 mm); Flow rate: 0.5 mL/min; Mobile phase: Phase A: 0.1% formic acid aqueous solution; Phase B:

0.1% formic acid acetonitrile solution. The gradient elution program was set as follows: 0−0.2 min 60%A; 0.2−1 min 60% → 5% A; 1−1.4 min 5% A; 1.4−1.41 min 5% A→60% A; 1.41−2.0 min 60% A.

Mass spectrometry analysis conditions (Triple Quad 5500, SCIEX): Mass spectrometry data were recorded using ESI, positive ion detection, and MRM scanning. The ion spray voltage and temperature were set at 5000 v and 550 °C, respectively. The curtain gas and CAD were set at 30 and 8 psi; gases 1 and 2 were set at 60 and 50 psi, respectively. The MS/MS parameters for ETO-4 and Tolbutamide (IS) are shown in Table 4.

**Table 4** Compound dependent parameters for ETO-4 and Tolbutamide.

| Compd. | Q1 Mass (Da) | Q3 Mass (Da) | Dwell time (msec) | DP (volts) | CE (volts) | CXP (volts) |
|---|---|---|---|---|---|---|
| ETO-4 | 361.2 | 112.9 | 120.0 | 47 | 20 | 13 |
| Tolbutamide (IS) | 271.1 | 172.2 | 120.0 | 70 | 18 | 20 |

Q1: parent ion; Q3: product ion; DP: declustering potential; CE: collision energy; CXP: collision cell exit potential.

*4.6.3. Tissue distribution metabolism experiment*

*4.6.3.1. Sample collection.* Blood collection method: Posterior extremity saphenous vein or other suitable veins. Anticoagulant: EDTA-K2. Sample type: Collect 200 μL of whole blood at each time point. Sample processing: Immediately after blood collection, protein precipitation was carried out with 5 times cold acetonitrile.

Tissue collection: After the blood collection of the mice is completed, the mice are buried in dry ice and frozen for about 1 min before collecting each tissue. After tissue collection, the residual blood on the surface is cleaned up, the surface moisture is absorbed, and then the samples are placed in pre-cooled sample tubes for weighing. After weighing, immediately store in dry ice for temporary storage, and then transfer each tissue to a −80 °C refrigerator for freezing storage. Sample preservation: All tissues should be labeled and stored in a freezer at −80 °C. Urine collection: After the intravenous injection of mice was completed, the mice were placed in a mouse metabolic cage for urine collection. The collection periods were before administration, 0−1, 1−4, and 4−24 h respectively.

*4.6.3.2. Samples pretreatment.* Pretreatment of whole blood samples: The whole blood samples that had been precipitated with 5 times the volume of cold acetonitrile protein was centrifuged at 36,670×*g* for 5 min at 4 °C. Six samples from the same group were mixed in equal volume, and 600 μL of the supernatant was taken and dried under $N_2$. The residue was dissolved in the initial mobile phase, and the supernatant was taken after centrifugation. Analysis using UHPLC-Q Exactive MS. Pretreatment of tissue samples: Each tissue was homogenized using PBS buffer (pH = 7.0) at a ratio of 1:4, and the six samples in the same group were mixed. Take 60 μL of the mixed tissue homogenate, add 250 μL of cold acetonitrile for protein precipitation, centrifuge at 14,000 rpm for 5 min at 4 °C, take 200 μL of the supernatant, blow dry under $N_2$, dissolve the residue in the initial mobile phase, centrifuge to take the supernatant, and analyze using UHPLC-Q Exactive MS. Pretreatment of urine samples: The urine samples of the same group were mixed in equal proportions and 200 μL was taken. 1000 μL of cold acetonitrile was added for precipitation. Centrifuged at 14,000 rpm for 5 min at 4 °C. 800 μL of the supernatant was taken and dried under $N_2$. The residue was dissolved in the initial mobile phase. After centrifugation and taking the supernatant, UHPLC-Q Exactive MS was used for analysis.

**Table 3** The improvements of the molecules generated by individual optimization algorithms.

| Algorithm | Improvement (mean) | Improvement (variance) | Success rate |
|---|---|---|---|
| SAGS | 8.74 | 6.09 | 82.25% |
| GA | 4.86 | 7.02 | 34.88% |
| MSO | 6.55 | 8.47 | 52.50% |
| JT-VAE | 0.21 | 0.721 | 46.40% |

*4.6.3.3. Measurement of samples by LC−MS.* The chromatographic column is Titank C18 (3 μm, 2.1 mm × 50 mm, Guangzhou Philomen Scientific Instrument Co., Ltd.). The column temperature is 40 °C. The flow rate is 0.35 mL/min. The liquid phase A is 0.1% formic acid water and phase B is 0.1% formic acid acetonitrile. The gradient elution program was set as follows: 0−4 min 99%A; 4−6 min 99% → 55% A; 6−8 min 55%→ 35% A; 8−14 min 35% A→5% A; 14−19.5 min 5% A; 19.5−20 min 5% → 99% A; 20−23 min 99% A. MS analysis was performed on Q Exactive HF high-resolution mass spectrometry. The scanning range is *m*/*z* 100−1500. Full scan spectra are obtained at a resolution of 30,000, and dd-MS2 data are obtained at a resolution of 15,000. Mass spectrometry detection is carried out in the positive ion mode. The parameters of the ion source are set as follows: Both the sheath gas and the auxiliary gas are nitrogen, with flow rates of 40 arb and 15 arb respectively; Capillary temperature: 275 °C Spray voltage: 3000 V; The temperature of the probe heater is 350 °C. The step-normalized collision energy (NCE) is set to 25, 35 and 45. The S-Lens RF level is 45.

### *4.7. In vivo efficacy and adverse events in mice*

*4.7.1. Hypnotic median effective dose measurement*

The hypnotic $ED_{50}$ of each compound was determined by up-and-down methods[47,48]. Loss of righting reflex test was performed to assess activity *in vivo*. Prepare each compound solution with normal saline and ensure all the compounds completely dissolve. Thirty ICR mice weighing 25 ± 2 g were randomly selected. Given the highest and lowest doses according to the pre-experimental results, the other three doses are set up in an isometric sequence. The test started with an intermediate dose. If the first mouse's righting reflex disappeared for more than 30 s, it was tagged positive, and the second mouse was given a lower dose. Contrarily, if the LORR time is less than 30 s or the righting reflex does not disappear, the second mouse was given a higher dose. The test was repeated until 8 cycles of positive-negative or negative-positive crosses were recorded.

$$ED_{50} = \mathrm{Log}_{10}^{-1}[X_0 + i(A/N \pm 0.5)] \quad (5)$$

where $X_0$ denotes the logarithmic dose of the middle dose group, $i$ denotes the logarithmic value of reciprocal dosage ratio, $A$ denotes the number multiplied by the interval from the maximum and minimum dose groups to the middle dose group, and $N$ denotes the

number of mice that had LORR. The 95% CI was calculated as Eq. (6):

$$95\%\ \mathrm{CI} = \mathrm{Log}_{10}^{-1}(\mathrm{X}_{50} \pm 1.96 \times \mathrm{Sx}_{50}) \quad (6)$$

where $X_{50}$ is the logarithmic dose of the $ED_{50}$, $Sx_{50}$ is the standard error, and the constant 1.96 reflects the 0.05 $\alpha$ level.

#### 4.7.2. *Pharmacodynamics of equivalent dose in mice*

Six male ICR mice weighing 25 ± 2 g were randomly selected. For each compound, a single dose of 2 × $ED_{50}$ was injected into the tail vein. Then, the onset time, RORR time and time to walk were recorded. Safety-related problems such as dyspnea, tremors, hypertonia, clonus, and convulsion were observed and recorded during the LORR.

#### 4.7.3. *Y-maze test*

The maze consists of three arms: a start arm, a novel arm, and an open arm. The test consists of two trials. The first time, the novel arm is blocked off and mice were placed into the maze. Then mice were administered either vehicle or test compounds (ETO-4 2 × $ED_{50}$, i.v.). When mice resumed normal walking, they were placed into the maze while the novel arm is unsealed. The time spent in the novel arm reflects spatial recognition memory[68], which were recorded by Smart v2.5 video tracking system (Panlab, Barcelona, Catalunya, Spain).

#### 4.7.4. *Open field test*

Before the experiment, the mice were adapted to the experimental room and chamber for 1 h. Then mice were administered either vehicle or test compounds (ETO-4 2 × $ED_{50}$, i.v.). When mice resumed normal walking, they were placed into the chamber to evaluate the effect of compounds on autonomic activity in mice. The distance travelled, average speed, maximum speed and resting time were recorded by Smart v2.5 video tracking system (Panlab, Barcelona, Catalunya, Spain)[69].

#### 4.7.5. *Rotarod test*

The rotarod test is divided into training stages and testing stages. On the first training day, mice were placed on the rotarod (ENV-575M, MED Associates, Fairfax, Vermont, USA) for 2 min with a low-speed rotation (4 rpm). Mice that could not stay on the rotarod for 2 min were excluded from this study. On the second day of training, the speed of rotarod system was set to start at 4 rpm to the maximum at 40 rpm. Mice were placed to five rounds of training every day for 4 consecutive days. Mice that could not stay on the rotor for 300 s were excluded from the study. On testing days, mice were placed on the rotarod before and after etomidate or ETO-4 (10 min) injection[70].

#### 4.7.6. *$GABA_A$ receptor antagonist study*

We pretreated the mice with bicuculline (competitive antagonist, 2.5, 5, 10 mg/kg i.p.) and picrotoxinin (noncompetitive antagonist, 2, 4, 8 mg/kg i.p.). ETO-4 (2 × $ED_{50}$) was given 1 min after that because we confirmed in preliminary experiments that convulsions induced by these drugs occur within 3 min after injection. The RORR time and the epilepsy score were recorded.

### 4.8. *In vivo efficacy in rats*

#### 4.8.1. *Determination of the minimum infusion rate*

A 22-gauge catheter was inserted into the tail vein to administer the drug infusion. The minimum infusion rate (MIR) for ETO-4 and etomidate was determined using the previously established method[71]. Based on the $ED_{50}$ of ETO-4 and etomidate in rats, they were induced under 2 × $ED_{50}$ and maintained with an initial dose of continuous infusion. A corneal reflex test was conducted to assess the level of anesthesia. Based on the response of the corneal reflex test, the infusion rate for the drug was adjusted by 10%, either increased or decreased. A "pair" was defined as a change in the direction of the response, either from negative to positive or positive to negative. The stimulation was then repeated at different infusion rates until five response pairs were recorded. The MIR was calculated as the average of these five mean values.

#### 4.8.2. *Continuous infusion and safety evaluation*

Rats were anesthetized under 2 × $ED_{50}$ of etomidate and ETO-4 and maintained with the minimum infusion rate calculated above. Etomidate and ETO-4 were infused continuously through tail vain. Meanwhile, the electroencephalogram was recorded. The heart rate, electrocardiogram and respiratory rate of rats were recorded by biological signal acquisition and processing system (BL-420N, Techman, Chengdu, China) per 5 min. The continuous infusion experiment lasted for half an hour, and the time when the rats resumed normal walking was observed and recorded after the drug was stopped. The heart rate at specific time points was directly imported and analyzed. The Q−T interval, P−R interval, and QRS complex duration at specific time points were manually measured. Q−T interval is measured from the starting point of the QRS wave and the end point of the T wave. P−R interval is measured from the starting point of the P wave and the starting point of the QRS complex wave. QRS complex duration is measured from the starting point of the QRS complex wave and the end point of the QRS complex wave. All data was processed and presented by GraphPad Prism 9.5.1.

#### 4.8.3. *Acute toxicity experiment*

14 days after infusion, rats' serum was collected for biochemical analysis. Heart, liver and kidney samples were fixed in 10% formalin for at least 48 h. The fixed samples were placed in plastic cassettes and dehydrated using an automated tissue processor. The processed tissues were embedded in paraffin wax and blocks trimmed and sectioned to about 5 × 4 μm size using a microtome. The tissue sections were mounted on glass slides using a hot plate and subsequently treated in the order of 100%, 90% and 70% ethanol for 2 min each. Finally, the tissue sections were rinsed in tap water, stained with H&E, and examined under a light microscope (Imager Z2, Zeiss).

### 4.9. *Serum corticosterone measurement*

Modified adrenocorticotropic hormone (ACTH)-stimulation test was used to evaluate the inhibitory effect of ETO-4 on adrenocortical function[42,72]. 15 male Sprague Dawley rats were randomly divided into 3 groups: etomidate, ETO-4 and vehicle ($n$ = 5 for each group). Dexamethasone at 0.5 mg/kg was administration to inhibit endogenous corticosterone. 2 h later, the test drugs were administration at 2 × $ED_{50}$, and 15 min later, $ACTH_{1-24}$ (25 μg/kg, Sigma−Aldrich Chemical Co, St. Louis, MO, USA) was administered to stimulate corticosterone production. Blood samples were drawn at 60 min after $ACTH_{1-24}$ administration. After clotting and centrifugation, the serum samples were collected. The concentration of serum corticosterone was measured using competitive ELISA kits (Cayman, MI, USA) and a 96-well plate reader. The measurements were taken within

15 min at a wavelength of 450 nm. The serum corticosterone concentration was calculated in strict accordance with the kit instructions. The assay sensitivity was 6.6 ng/mL.

### 4.10. Methods of electrophysiological recording assay

#### 4.10.1. $GABA_A(\alpha1\beta2\gamma2)$ patch clamp assay

Electrophysiological recordings of $GABA_A(\alpha1\beta2\gamma2)$ channels were performed by a EPC10 amplifier (HEKA, Germany) connected with PatchMaster software (HEKA, Germany). For voltage-clamp recording of $GABA_A(\alpha1\beta2\gamma2)$, the extracellular solution contained (in mmol/L): 137 NaCl, 4 KCl, 1.8 $CaCl_2$, 1 $MgCl_2$, 10 Glucose, 10 HEPES. pH was adjusted to 7.4 with NaOH. The intracellular solution contained (in mmol/L): 140 CsCl, 5 EGTA,10 HEPES. pH was adjusted to 7.2 with CsOH. NaCl, CsCl, $MgCl_2$, $CaCl_2$, EGTA, $Na_2ATP$, D-glucose, NaOH, CsOH and HEPES were purchased from Sigma (St Louis, MO, USA). After establishing the whole-cell configuration, $GABA_A$ currents were recorded at −70 mV, and peak GABA currents were recorded, sprayed on the cell surface for 10−15 s using gravity administration and cumulative dosing, and the same cell was cumulatively dosed with negative (0.1% DMSO), GABA 3 μmol/L, and a mixture of GABA 3 μmol/L and tested compounds (from low to high).

#### 4.10.2. hERG patch clamp assay

The hERG-HKE293 (NM_000238) stably transfected cell line should be maintained within 70% of the maximum density in the logarithmic growth phase before the start of electrophysiology experiments. Adjusted the cell concentration then to $2 \times 10^3$/mL, respectively, take 300 μL of cell solution (resistant Puromycine 2 μg/mL) inoculated into the cell crawler of 24-well plate, and wait for the cells to be well adhered to the wall. hERG extracellular solution (mmol/L): 137 NaCl, 4 KCl, 10 HEPES, 10 D-glucose, 1 $MgCl_2 \cdot 6H_2O$, 2 $CaCl_2 \cdot 2H_2O$, and NaOH adjusted to pH = 7.4. hERG intracellular fluid (mmol/L): 20 KCl, 120 K-Aspartic, 10 HEPES, 10 EGTA, 5 Mg-ATP, KOH adjusted pH = 7.2. Stimulation procedure: clamp voltage was −80 mV, depolarized to +40 mV for 4000 ms, then repolarized to −50 mV for 4000 ms, tail current could be induced, and the current was recorded every 15 s. The current was recorded at the same time. At room temperature, the hERG potassium channel current before dosing was recorded. After the control current value reached a steady state, *i.e.*, after the nearest four consecutive current recording lines overlapped, the cumulative dosing method was used to sequentially add the negative (0.1% DMSO), and the five compound concentrations (from low to high).

### 4.11. The inhibition assay of 11β-hydroxylase

G402-puro-human CYP11B1 cells were seeded in 96 well plate and incubate for 24 h before compound treatment. We refreshed medium with DMEM/F12 medium containing 2.5% charcoal treated FCS. The cell plates were added with 5 μL of positive compounds and the compound to be tested working solution, and incubated in a cell incubator at 37 °C, 5% $CO_2$, and 95% relative humidity for 1 h. After then 1 μM substrate 11-DC was added into cell, incubate for another 16 h. After 16 h, the cell plates were mixed for 3−5 min and centrifuged at room temperature at 3220×*g* for 5 min. Take 50 μL cell supernatant from the cells and add it to the termination solution containing 200 μL internal standard. After mixed for 3−5 min, centrifuge at 4 °C at 3220×*g* for 30 min. Then 100 μL supernatant was transferred to an analysis plate containing 100 μL volume $H_2O$ for LC−MS/MS analysis. The metabolites of specific substrates were detected by LC−MS/MS. The peak area ratio of the sample to the internal standard was calculated by using the internal standard method. The inhibition percentage was calculated by using the ratio or the $IC_{50}$ was fitted using the XLfit 4 parameter formula.

### 4.12. The inhibition assay of CYP450

Add 1 μL of test compound and 179 μL of liver microsomes into the Incubation Plate in duplicate as indicated. Pre-warm the incubation plate at 37 °C for 5 min. Add 20 μL of 10 mmol/L NADPH solution to start the reaction. Add 300 μL methanol with IS to the Incubation Plate at the designated time to stop the reaction. Centrifuge the sample plate at 3220×*g* for 40 min. Transfer 100 μL of the supernatant to an analysis plate containing a proper volume of $H_2O$ for LC−MS/MS analysis.

### 4.13. Cell viability test

Firstly, the cell suspension was prepared during the logarithmic growth phase. After adjusting to an appropriate concentration, it was seeded into 96-well plates at a volume of 100 μL per well, and blank controls (culture medium only), negative controls (cells only), and experimental groups containing different concentrations of drugs were set up. The inoculated cells were pre-cultured in a 37 °C, 5% $CO_2$ incubator for 24 h to allow them to adhere and recover. Subsequently, the experimental group was replaced with drug-containing medium, while the control group was replaced with fresh medium. The drug treatment continued for 24 h. Before the treatment is completed, restore the CCK-8 reagent to room temperature and add it to each well at a ratio of 10% of the culture medium volume. Gently mix well and incubate in the incubator in the dark for 1−4 h to carry out the color reaction. Finally, the absorbance values of each well were measured at a wavelength of 450 nm using an enzyme-linked immunosorbent assay (ELISA) reader, and the relative cell viability of each experimental group was calculated through Eq. (7):

$$\text{Cell viability}\,(\%) = (\text{OD experimental group} - \text{OD blank group}) / (\text{OD control group} - \text{OD blank group}) \times 100 \quad (7)$$

### 4.14. Electroencephalogram recording and analysis

Mice were induced to anesthetic states in an induction chamber with 1.5% isoflurane and then transferred and secured to a stereotaxic frame. The optical fiber and electrodes were secured to the skull surface and sealed with dental acrylic. The mice recovered for at least 7 days after the operation. On the day of recording, the mice were first placed in the recording box to adapt for 20 min, with the temperature maintained at 25 °C, and allowed to move freely. After adaptation, the mice were connected to the EEG/EMG system and moved freely. The baseline of the electroencephalogram was recorded for 4 min first. When the drug anesthesia began, the time was recorded and the electroencephalogram recording continued until the mice recovered. All electroencephalogram signals were recorded at a frequency of 400 Hz using Pinnacle's three-channel tethered EEG/EMG systems

(Pinnacle technology, USA). The signals were filtered within the frequency range of 0.5 to 30 Hz. Electroencephalogram (EEG) inhibition is defined as occurring when the amplitude is between −20 and 20 μV and lasts for more than 0.1 s. Calculate the cumulative inhibition time, that is, the total of each single inhibition time within 4 min after the start of drug anesthesia.

### *4.15. Statistical analysis*

Statistical analyses were analyzed using GraphPad 9.5.1 and presented as mean ± standard error of mean (SEM). The level of statistical significance was set at $P < 0.05$. Two-tailed paired Student's *t*-tests and one-way or two-way ANOVA followed by Tukey post tests were used to examine statistical significance. n.s. indicates no significance. $*P < 0.05$, $**P < 0.01$, $***P < 0.001$, $****P < 0.0001$.

## Acknowledgments

The authors gratefully acknowledge the National Natural Science Foundation of China (82425054 and 82273784), Brain Science and Brain-like Intelligence Technology-National Science and Technology Major Project (2025ZD0214904, China), Innovation Drug Research and Development National Science and Technology Major Project (2025ZD1801600, China), National Natural Science Foundation of China (82171263), the Science and Technology Major Project of Tibetan Autonomous Region of China (XZ202201ZD0001G04-LH), Sichuan Science and Technology Program (2023YFS0142, China), the 1.3.5 Project for Disciplines of Excellence, West China Hospital, Sichuan University (ZYGD25002, China), Postdoctoral Fellowship Program of CPSF (GZB20250827, China), and Postdoctor Research Fund of West China Hospital, Sichuan University (2025HXBH107, China). We thank Feijing Su, Qifeng Liu and Jie Tu at the Core Facilities of West China Hospital for their help with NMR measurements. The computations in this paper were supported by the High-Performance Computing platform at West China Biomedical Big Data Center, West China Hospital, Sichuan University.

## Author contributions

Yi Zhao, Wei Ai, Jieyu Zhao and Xi Yang contributed equally. All authors have given approval to the final version of the manuscript. Bowen Ke: conceptualization, funding acquisition, revision of original draft, Jun Yang and Xianggen Liu: conceptualization. Yi Zhao, Wei Ai, Jieyu Zhao and Xi Yang: data acquisition, data curation, formal analysis, investigation, writing of original draft. Wencheng Liu, Yaru Ma, Jianrui Mou, Ao Hai, Ran Ji, Jin Liu. and Zhengbo Huang helped to perform specific experiments. Yu Gan, Zhuang Miao and Shilong Hu helped to draw figures in this study.

## Conflicts of interest

The authors declare that they have no known competing financial interests or personal relationships that could have appeared to influence the work reported in this paper.

## Appendix A. Supporting information

Supporting information to this article can be found online at https://doi.org/10.1016/j.apsb.2026.01.008.

## References

1. Doenicke A. Etomidate, a new intravenous hypnotic. *Acta Anaesthesiol Belg* 1974;**25**:307−15.
2. Kay B. A dose-response relationship for etomidate, with some observations on cumulation. *Br J Anaesth* 1976;**48**:213−6.
3. Čižmáriková R, Habala L, Markulia M. General intravenous anesthetics−pharmacodynamics, pharmacokinetics and chiral properties. *Ces Slov Farm* 2023;**72**:155−64.
4. Zed PJ, Abu-Laban RB, Harrison DW. Intubating conditions and hemodynamic effects of etomidate for rapid sequence intubation in the emergency department: an observational cohort study. *Acad Emerg Med* 2006;**13**:378−83.
5. Knack SKS, Prekker ME, Moore JC, Klein LR, Atkins AH, Miner JR, et al. The effect of ketamine versus etomidate for rapid sequence intubation on maximum sequential organ failure assessment score: a randomized clinical trial. *J Emerg Med* 2023;**65**:e371−82.
6. Lee JM, Min G, Lee JM, Kim SH, Choi HS, Kim ES, et al. Efficacy and safety of etomidate-midazolam for screening colonoscopy in the elderly: a prospective double-blinded randomized controlled study. *Medicine (Baltim)* 2018;**97**:e10635.
7. Wagner RL, White PF, Kan PB, Rosenthal MH, Feldman D. Inhibition of adrenal steroidogenesis by the anesthetic etomidate. *N Engl J Med* 1984;**310**:1415−21.
8. Allolio B, Stuttmann R, Leonhard U, Fischer H, Winkelmann W. Adrenocortical suppression by a single induction dose of etomidate. *Klin Wochenschr* 1984;**62**:1014−7.
9. Ledingham IM, Watt I. Influence of sedation on mortality in critically ill multiple trauma patients. *Lancet* 1983;**1**:1270.
10. Lambert A, Mitchell R, Frost J, Ratcliffe JG, Robertson WR. Direct *in vitro* inhibition of adrenal steroidogenesis by etomidate. *Lancet* 1983;**2**:1085−6.
11. Fellows IW, Bastow MD, Byrne AJ, Allison SP. Adrenocortical suppression in multiply injured patients: a complication of etomidate treatment. *Br Med J (Clin Res Ed)* 1983;**287**:1835−7.
12. Morris C, McAllister C. Etomidate for emergency anaesthesia; mad, bad and dangerous to know?. *Anaesthesia* 2005;**60**:737−40.
13. Chan CM, Mitchell AL, Shorr AF. Etomidate is associated with mortality and adrenal insufficiency in sepsis: a meta-analysis. *Crit Care Med* 2012;**40**:2945−53.
14. Kim JJ, Gharpure A, Teng J, Zhuang Y, Howard RJ, Zhu S, et al. Shared structural mechanisms of general anaesthetics and benzodiazepines. *Nature* 2020;**585**:303−8.
15. Jin B, Pang X, Zang Q, Ga M, Xu J, Luo Z, et al. Spatiotemporally resolved metabolomics and isotope tracing reveal CNS drug targets. *Acta Pharm Sin B* 2023;**13**:1699−710.
16. Shalabi AR, Yu Z, Zhou X, Jounaidi Y, Chen H, Dai J, et al. A potent photoreactive general anesthetic with novel binding site selectivity for GABAA receptors. *Eur J Med Chem* 2020;**194**:112261.
17. Shanmugasundararaj S, Zhou X, Neunzig J, Bernhardt R, Cotten JF, Ge R, et al. Carboetomidate: an analog of etomidate that interacts weakly with 11$\beta$-hydroxylase. *Anesth Analg* 2013;**116**:1249−56.
18. Hahner S, Stuermer A, Kreissl M, Reiners C, Fassnacht M, Haenscheid H, et al. [$^{123}$I]Iodometomidate for molecular imaging of adrenocortical cytochrome P450 family 11B enzymes. *J Clin Endocrinol Metab* 2008;**93**:2358−65.
19. de Jong FH, Mallios C, Jansen C, Scheck PA, Lamberts SW. Etomidate suppresses adrenocortical function by inhibition of 11 beta-hydroxylation. *J Clin Endocrinol Metab* 1984;**59**:1143−7.
20. Liu W, Li Z, Chu S, Ma X, Wang X, Jiang M, et al. Atractylenolide-I covalently binds to CYP11B2, selectively inhibits aldosterone synthesis, and improves hyperaldosteronism. *Acta Pharm Sin B* 2022;**12**:135−48.

21. Dzialach L, Sobolewska J, Respondek W, Wojciechowska-Luzniak A, Kuca P, Witek P. Is there still a place for etomidate in the management of Cushing's syndrome?. The experience of a single center of low-dose etomidate and combined etomidate-osilodrostat treatment in severe hypercortisolemia. *Endocrine* 2025;**87**:1305−13.
22. Pejo E, Santer P, Wang L, Dershwitz P, Husain SS, Raines DE. γ-Aminobutyric acid type A receptor modulation by etomidate analogs. *Anesthesiology* 2016;**124**:651−63.
23. Zolle IM, Berger ML, Hammerschmidt F, Hahner S, Schirbel A, Peric-Simov B. New selective inhibitors of steroid 11beta-hydroxylation in the adrenal cortex. Synthesis and structure−activity relationship of potent etomidate analogues. *J Med Chem* 2008;**51**:2244−53.
24. Gay SC, Sun L, Maekawa K, Halpert JR, Stout CD. Crystal structures of cytochrome P450 2B4 in complex with the inhibitor 1-biphenyl-4-methyl-1*H*-imidazole: ligand-induced structural response through alpha-helical repositioning. *Biochemistry* 2009;**48**:4762−71.
25. Roumen L, Sanders MPA, Pieterse K, Hilbers PAJ, Plate R, Custers E, et al. Construction of 3D models of the CYP11B family as a tool to predict ligand binding characteristics. *J Comput Aided Mol Des* 2007; **21**:455−71.
26. Cotten JF, Forman SA, Laha JK, Cuny GD, Husain SS, Miller KW, et al. Carboetomidate: a pyrrole analog of etomidate designed not to suppress adrenocortical function. *Anesthesiology* 2010;**112**:637−44.
27. Cotten JF, Le Ge R, Banacos N, Pejo E, Husain SS, Williams JH, et al. Closed-loop continuous infusions of etomidate and etomidate analogs in rats: a comparative study of dosing and the impact on adrenocortical function. *Anesthesiology* 2011;**115**:764−73.
28. Jiang JH, Xu XQ, Jiang WG, Wang T, Liu X, Zeng LG, et al. Discovery of the EL-0052 as a potential anesthetic drug. *Comput Struct Biotechnol J* 2021;**19**:710−8.
29. Xu X, Wei Y, Dong Y, Qiu Y, Mei Z, Wang K, et al. A novel etomidate analog EL-0052 retains potent hypnotic effect and stable hemodynamics without suppressing aadrenocortical function. *J Pharmacol Exp Therapeut* 2021;**379**:324−30.
30. Forman SA. Clinical and molecular pharmacology of etomidate. *Anesthesiology* 2011;**114**:695−707.
31. Fragen RJ, Shanks CA, Molteni A, Avram MJ. Effects of etomidate on hormonal responses to surgical stress. *Anesthesiology* 1984;**61**: 652−6.
32. Wanscher M, Tønnesen E, Hüttel M, Larsen K. Etomidate infusion and adrenocortical function. A study in elective surgery. *Acta Anaesthesiol Scand* 1985;**29**:483−5.
33. Vinclair M, Broux C, Faure P, Brun J, Genty C, Jacquot C, et al. Duration of adrenal inhibition following a single dose of etomidate in critically ill patients. *Intensive Care Med* 2008;**34**:714−9.
34. Valk BI, Absalom AR, Meyer P, Meier S, den Daas I, van Amsterdam K, et al. Safety and clinical effect of i.v. infusion of cyclopropyl-methoxycarbonyl etomidate (ABP-700), a soft analogue of etomidate, in healthy subjects. *Br J Anaesth* 2018;**120**:1401−11.
35. Husain SS, Pejo E, Ge R, Raines DE. Modifying methoxycarbonyl etomidate inter-ester spacer optimizes *in vitro* metabolic stability and *in vivo* hypnotic potency and duration of action. *Anesthesiology* 2012; **117**:1027−36.
36. Valk BI, McGrath M, Lehoux D, Zerler B, Marota JJA, Raines DE. Toxicologic and inhibitory receptor actions of the etomidate analog ABP-700 and its metabolite CPM-acid. *Anesthesiology* 2019;**131**: 287−304.
37. Yang J, Kang Y, Wang B, Yang L, Liu J, Zhang W. Metabolite-inactive etomidate analogues alleviating suppression on adrenal function in Beagle dogs. *Eur J Pharmaceut Sci* 2017;**99**:343−9.
38. Liu X, Li P, Meng F, Zhou H, Zhong H, Zhou J, et al. Simulated annealing for optimization of graphs and sequences. *Neurocomputing* 2021;**465**:310−24.
39. Biau G. Analysis of a random forests model. *J Mach Learn Res* 2012; **13**:1063−95.
40. Yin Q, Yang Y, Liu J, Li L, Yang X, Diao L, et al. Phase 1 single-centre placebo- and etomidate-controlled study in healthy volunteers to assess safety, tolerability, clinical effects, and pharmacokinetics of intravenous methoxyethyl etomidate hydrochloride (ET-26). *Br J Anaesth* 2025;**134**:80−8.
41. Jiang X, Yin Q, Deng X, Zhang W, Zhang W, Liu J. Advance of a new etomidate analogue — methoxyethyl etomidate hydrochloride (ET-26) for anesthesia induction in surgical patients. *APS* 2024;**2**:22.
42. Wang B, Yang J, Chen J, Kang Y, Yang LH, Liu J, et al. An etomidate analogue with less adrenocortical suppression, stable hemodynamics, and improved behavioral recovery in rats. *Anesth Analg* 2017;**125**: 442−50.
43. Ruthenbeck A, Elgaher WAM, Haupenthal J, Hartmann RW, Meier C. Bacterial RNAP inhibitors: synthesis and evaluation of prodrugs of aryl-ureidothiophene-carboxylic acids. *ChemistrySelect* 2017;**2**: 11899−905.
44. Atucha E, Hammerschmidt F, Zolle I, Sieghart W, Berger ML. Structure−activity relationship of etomidate derivatives at the GABA (A) receptor: comparison with binding to 11beta-hydroxylase. *Bioorg Med Chem Lett* 2009;**19**:4284−7.
45. Sha X. *Inventor; Nanjing Ruizhi Biological Medicine Co., Ltd., assignee. Preparation of ornidazole ester prodrug, its pharmaceutical composition and application as antibacterial agents. CN114478391 A May13*. 2022. p. 2022.
46. Tanious MK, Beutler SS, Kaye AD, Urman RD. New hypnotic drug development and pharmacologic considerations for clinical anesthesia. *Anesthesiol Clin* 2017;**35**:e95−113.
47. Dixon WJ. Staircase bioassay: the up-and-down method. *Neurosci Biobehav Rev* 1991;**15**:47−50.
48. Oron AP, Souter MJ, Flournoy N. Understanding research methods: up-and-down designs for dose-finding. *Anesthesiology* 2022;**137**: 137−50.
49. Evoy KE, Morrison MD, Saklad SR. Abuse and misuse of pregabalin and ggabapentin. *Drug* 2017;**77**:403−26.
50. Irifune M, Sugimura M, Takarada T, Maeoka K, Shimizu Y, Dohi T, et al. Propofol anaesthesia in mice is potentiated by muscimol and reversed by bicuculline. *Br J Anaesth* 1999;**83**:665−7.
51. Irifune M, Takarada T, Shimizu Y, Endo C, Katayama S, Dohi T, et al. Propofol-induced anesthesia in mice is mediated by gamma-aminobutyric acid-A and excitatory amino acid receptors. *Anesth Analg* 2003;**97**:424−9.
52. Pressly B, Vasylieva N, Barnych B, Singh V, Singh L, Bruun DA, et al. Comparison of the toxicokinetics of the convulsants picrotoxinin and tetramethylenedisulfotetramine (TETS) in mice. *Arch Toxicol* 2020; **94**:1995−2007.
53. Zhang L, Fan S, Zhang J, Fang K, Wang L, Cao Y, et al. Electroencephalographic dynamics of etomidate-induced loss of consciousness. *BMC Anesthesiol* 2021;**21**:108.
54. Ching S, Purdon PL, Vijayan S, Kopell NJ, Brown EN. A neurophysiological−metabolic model for burst suppression. *Proc Natl Acad Sci* 2012;**109**:3095−100.
55. Liu W, Luo C, Wang H, Fanwang M. *A benchmarking dataset with 2440 organic molecules for volume distribution at steady state*. 2022. Available from: https://github.com/da-wen-er/VDss.
56. Li P, Wang J, Qiao Y, Chen H, Yu Y, Yao X, et al. An effective self-supervised framework for learning expressive molecular global representations to drug discovery. *Brief Bioinform* 2021;**22**. bbab109.
57. Jin W, Barzilay R, Jaakkola T. Junction tree variational autoencoder for molecular graph generation. Proceedings of the 35th international conference on machine learning; 2018; proceedings of machine learning research. Available from: http://doi.10.480/arXiv.1802.04364.
58. Irwin JJ, Sterling T, Mysinger MM, Bolstad ES, Coleman RG. ZINC: a free tool to discover chemistry for biology. *J Chem Inf Model* 2012; **52**:1757−68.
59. Winter R, Montanari F, Steffen A, Briem H, Noé F, Clevert DA. Efficient multi-objective molecular optimization in a continuous latent space. *Chem Sci* 2019;**10**:8016−24.
60. Brixius-Anderko S, Scott EE. Structure of human cortisol-producing cytochrome P450 11B1 bound to the breast cancer drug fadrozole provides insights for drug design. *J Biol Chem* 2018;**294**:453−60.

61. Jo S, Kim T, Iyer VG, Im W. CHARMM-GUI: a web-based graphical user interface for CHARMM. *J Comput Chem* 2008;**29**:1859−65.
62. Best RB, Zhu X, Shim J, Lopes PEM, Mittal J, Feig M, et al. Optimization of the additive CHARMM all-atom protein force field targeting improved sampling of the backbone $\phi$, $\psi$ and side-chain $\chi(1)$ and $\chi(2)$ dihedral angles. *J Chem Theor Comput* 2012;**8**:3257−73.
63. Klauda JB, Venable RM, Freites JA, O'Connor JW, Tobias DJ, Mondragon-Ramirez C, et al. Update of the CHARMM all-atom additive force field for lipids: validation on six lipid types. *J Phys Chem B* 2010;**114**:7830−43.
64. Valdés-Tresanco MS, Valdés-Tresanco ME, Valiente PA, Moreno E. gmx_MMPBSA: a new tool to perform end-state free energy ggalculations with GROMACS. *J Chem Theor Comput* 2021;**17**:6281−91.
65. Abraham MJ, Murtola T, Schulz R, Páll S, Smith JC, Hess B, et al. GROMACS: high performance molecular simulations through multi-level parallelism from laptops to supercomputers. *SoftwareX* 2015;**1**:19−25.
66. Song S, Sun D, Wang H, Wang J, Yan H, Zhao X, et al. Full-profile pharmacokinetics, anticancer activity and toxicity of an extended release trivalent PEGylated irinotecan prodrug. *Acta Pharm Sin B* 2023;**13**:3444−53.
67. Sobczak A, Teżyk A, Szyndlarewicz J, Ziarniak J, Świątek P, Malinka W. New fluphenazine analogue with antimutagenic and anti-multidrug resistance activity-degradation profile and stability-indicating method. *Med Chem Res* 2017;**26**:2443−51.
68. Wang P, Shao Y, Al-Nusaif M, Zhang J, Yang H, Yang Y, et al. Pathological characteristics of axons and alterations of proteomic and lipidomic profiles in midbrain dopaminergic neurodegeneration induced by WDR45-deficiency. *Mol Neurodegener* 2024;**19**:62.
69. Ai X, Wu Y, Lu W, Zhang X, Zhao L, Tu P, et al. A precise microfluidic assay in single-cell profile for screening of transient receptor potential channel modulators. *Adv Sci (Weinh)* 2020;**7**:2000111.
70. Jin S, Cao Q, Yang F, Zhu H, Xu S, Chen Q, et al. Brain ethanol metabolism by astrocytic ALDH2 drives the behavioural effects of ethanol intoxication. *Nat Metab* 2021;**3**:337−51.
71. Jiang J, Wang B, Zhu Z, Yang J, Liu J, Zhang W. Minimum infusion rate and adrenocortical function after continuous infusion of the novel etomidate analog ET-26-HCl in rats. *PeerJ* 2017;**5**:e3693.
72. Pejo E, Cotten JF, Kelly EW, Le Ge R, Cuny GD, Laha JK, et al. *In vivo* and *in vitro* pharmacological studies of methoxycarbonyl-carboetomidate. *Anesth Analg* 2012;**115**:297−304.